

AN ABSTRACT OF THE THESIS OF

Benjamin E. Waters for the degree of Master of Science in

Electrical and Computer Engineering presented on July 2, 2012.

Title: Physical Vapor Deposition of Novel Thin-Film Solar Absorbers

Abstract approved: _____

John F. Wager

Current leading thin-film solar cell technologies, i.e., cadmium telluride (CdTe) and copper indium gallium diselenide (CIGS), employ elements which are either toxic (Cd), or rare and/or expensive (In, Te, Ga, and Cd). The aim of this thesis is to investigate new, abundant, non-toxic p-type semiconductors for potential solar absorber application. Two ternary chalcogenides, Cu_3PSe_4 and CuTaS_3 , were selected for their attractive calculated optical absorption properties. Thin films of both materials were synthesized using physical vapor deposition (PVD) techniques in conjunction with post-deposition annealing. Cu_3PSe_4 appears promising for solar absorber applications, with a measured optical bandgap of 1.2 eV, an absorption coefficient (α) reaching 10^5 cm^{-1} , Hall mobilities of $19.8\text{--}30.3 \text{ cm}^2/\text{V}\cdot\text{s}$, and carrier concentrations of $3.3\text{--}4.9 \times 10^{16} \text{ cm}^{-3}$. Optical characterization of CuTaS_3 thin-films showed a rapid turn-on of absorption, with α exceeding 10^5 cm^{-1} within 0.5 eV of the bandgap. To date, reproducible synthesis of CuTaS_3 thin films has been problematic. Moreover, these films are insulating and thus not yet appropriate for thin-film solar cell absorber applications.

©Copyright by Benjamin E. Waters

July 2, 2012

All Rights Reserved

Physical Vapor Deposition of Novel Thin-Film Solar Absorbers

by

Benjamin E. Waters

A THESIS

submitted to

Oregon State University

in partial fulfillment of
the requirements for the
degree of

Master of Science

Presented July 2, 2012
Commencement June 2013

Master of Science thesis of Benjamin E. Waters presented on July 2, 2012.

APPROVED:

Major Professor, representing Electrical and Computer Engineering

Director of the School of Electrical Engineering and Computer Science

Dean of the Graduate School

I understand that my thesis will become part of the permanent collection of Oregon State University libraries. My signature below authorizes release of my thesis to any reader upon request.

Benjamin E. Waters, Author

In memory of Adam Nathaniel Yauch

August 5, 1964 – May 4, 2012

TABLE OF CONTENTS

	<u>Page</u>
1. INTRODUCTION	1
2. LITERATURE REVIEW	3
2.1 Introduction to solar cells	3
2.1.1 Device structure	3
2.1.2 Ideal solar cell operation	6
2.1.3 Non-ideal solar cell operation	8
2.1.4 P-i-n solar cells	14
2.1.5 Multi-junction solar cells	15
2.1.6 Device characterization	17
2.1.7 Solar spectrum radiation	21
2.1.8 Ohmic contact theory and formation	22
2.2 Thin-film solar cell materials	30
2.2.1 Cadmium telluride (CdTe)	31
2.2.2 Copper indium gallium diselenide (CIGS)	31
2.2.3 Hydrogenated amorphous silicon (a-Si:H)	32
2.3 Conclusion	33
3. EXPERIMENTAL TOOLS AND TECHNIQUES	36
3.1 Thin film deposition and processing	36
3.1.1 Pulsed laser deposition of thin films	36
3.1.2 Electron-beam evaporation	40
3.1.3 Post-deposition annealing	43
3.2 Thin-film characterization	44
3.2.1 X-ray diffraction	44
3.2.2 Hall effect measurement	45
3.2.3 Optical transmission and reflection	48
3.2.4 X-ray reflectivity (XRR)	49
3.2.5 Spectroscopic ellipsometry (SE)	50
3.2.6 Photoelectrochemical (PEC) cell measurements	53

TABLE OF CONTENTS (Continued)

	<u>Page</u>
3.3 Conclusion	54
4. Cu ₃ PSe ₄ THIN-FILMS	56
4.1 Introduction	56
4.2 Experiment.....	60
4.2.1 Pulsed laser deposition parameters	60
4.2.2 Post-deposition anneals in P and Se	63
4.2.3 Effect of different substrate materials	63
4.2.4 Post-deposition anneals with P ₄ Se ₃ powder.....	66
4.3 Characterization of thin-films	66
4.3.1 Optical transmission and reflection.....	67
4.3.2 Electrical characterization	67
4.4 Conclusion	69
5. CuTaS ₃ THIN FILMS	70
5.1 Introduction	70
5.2 Experiment.....	73
5.2.1 Sulfurization of Cu-Ta thin-film precursors	73
5.2.2 Electron-beam evaporation of CuTaS ₃ pellets.....	74
5.3 Results.....	76
5.4 Conclusion	77
6. CONCLUSIONS AND RECOMMENDATIONS FOR FUTURE WORK	78
6.1 Conclusions	78
6.1.1 Cu ₃ PSe ₄	78
6.1.2 CuTaS ₃	79

TABLE OF CONTENTS (Continued)

	<u>Page</u>
6.2 Recommendations for future work	79
6.2.1 Cu_3PSe_4	79
6.2.2 CuTaS_3	80
BIBLIOGRAPHY	81

LIST OF FIGURES

<u>Figure</u>	<u>Page</u>
2.1 Structure of a monocrystalline silicon solar cell.	4
2.2 Thin-film solar cell stack. [1]	5
2.3 Energy band diagrams for a solar cell (a) in the dark, and (b) under illumination.	7
2.4 Equivalent circuit for an ideal solar cell (within dashed lines) connecting to an external load R_L	8
2.5 Ideal solar cell I-V curves under dark and illuminated conditions.	9
2.6 Current-voltage (I-V) and power-voltage (P-V) curve for an ideal solar cell. [2]	10
2.7 Energy band diagrams of (a) radiative, (b) Auger, and (c) Shockley-Read-Hall recombination processes.	11
2.8 Equivalent circuit model for a non-ideal solar cell. Non-ideal elements are contained by the dashed lines.	12
2.9 Effect of (a) series and (b) shunt resistance on solar cell I-V curves.	13
2.10 Energy band diagram for a p-i-n solar cell.	15
2.11 Triple-junction solar cell structure. [3]	16
2.12 Ideal solar cell equivalent circuit under (a) short-circuit, and (b) open-circuit conditions.	18
2.13 Non-ideal solar cell equivalent circuit under (a) short-circuit, and (b) open-circuit conditions.	19
2.14 AM0 and AM1.5 solar spectra. [4]	22
2.15 Solar cell efficiency vs. band gap for the AM1.5 spectrum. [4]	23
2.16 Energy band diagrams for (a) metal, and (b) p-type semiconductor materials before being joined together.	24
2.17 Energy band diagram for an ideal ohmic contact formed with a p-type semiconductor.	25
2.18 Energy band diagram for an ideal rectifying contact formed with a p-type semiconductor.	26

LIST OF FIGURES (Continued)

<u>Figure</u>	<u>Page</u>
2.19 Energy band diagram showing Schottky barrier formation from the presence of surface states on an n-type semiconductor.	28
2.20 Energy band diagram showing (a) field emission, (b) thermionic-field emission, and (c) thermionic emission across a Schottky barrier formed with a p-type semiconductor.....	29
2.21 Solar cell stacks for (a) CdTe, (b) CIGS, and (c) a-Si:H.	30
3.1 Pulsed laser deposition system schematic. [5] Substrate rotation is also present in some systems.....	37
3.2 Diagram of an electron-beam evaporator. [6]	41
3.3 Diffraction of x-rays by a crystalline structure. [7]	45
3.4 Example XRD diffraction patterns for crystalline and amorphous solids. Intensity is plotted vs. 2θ by convention. [7]	46
3.5 Experimental configuration for the Hall effect measurement. [8]	46
3.6 Experimental setup for measuring transmitted and reflected intensities... ..	48
3.7 X-ray reflection at the thin-film surface and film-substrate interface.	50
3.8 Plot of x-ray reflectivity vs. incidence angle. [9]	51
3.9 Variable angle spectroscopic ellipsometer tool schematic. An external control box (not shown) controls the detector unit and sample stage rotation.	52
3.10 Overhead view of the variable angle spectroscopic ellipsometer, showing the reflection of light incident on the sample.....	52
3.11 Energy band diagram of a PEC cell with an n-type photoelectrode and electrolyte containing the redox couple A, A^-	54
4.1 Enargite crystal structure for Cu_3PSe_4 , showing Cu (orange), P (red), and Se (yellow) atoms.	58
4.2 Calculated energy band structure for Cu_3PSe_4 . [10]	58

LIST OF FIGURES (Continued)

<u>Figure</u>	<u>Page</u>
4.3 Calculated absorption coefficient for Cu_3PSe_4 (red) along with experimental data for GaAs (brown dashed) and CIGS (green dashed). The real (solid) and imaginary (long-dashed) parts of the dielectric function ϵ are also shown. [10]	59
4.4 Calculated spectroscopically limited maximum efficiency (SLME) versus absorber layer thickness for Cu_3PSe_4 solar cells. [11]	59
4.5 Measured XRD spectra for films deposited by PLD at various substrate temperatures. Laser fluence was 1 J/cm^2 . Cu_7PSe_6 (red) and $\text{Cu}_{1.8}\text{Se}$ (green) reference spectra are shown for comparison.	61
4.6 Measured XRD spectra for films deposited by PLD at various laser fluences on 300°C substrates. Cu_7PSe_6 (red) and $\text{Cu}_{1.8}\text{Se}$ (green) reference spectra are shown for comparison.....	62
4.7 Measured XRD spectrum for a Cu_3PSe_4 thin-film sample (blue) and the Cu_3PSe_4 reference spectrum (red) for comparison. The sample was deposited by PLD with a 300°C substrate temperature and laser fluence of 1 J/cm^2 , and annealed at 450°C in a P and Se background.	64
4.8 Measured XRD spectra for samples annealed at different temperatures. .	67
4.9 Measured absorption coefficient for a Cu_3PSe_4 thin-film sample.	68
5.1 Crystal structure for CuTaS_3 showing Cu (small white circles), S (large white circles), and Ta (black dots). Large channels in the $[010]$ direction are visible. [12]	71
5.2 Calculated absorption coefficient for CuTaS_3 . [11]	71
5.3 Calculated SLME for CuTaS_3 . [11]	72
5.4 Process flow of sulfurization of CuTa precursors, showing (a) CuTa multilayers, (b) CuTa quasi-alloy, and (c) tube furnace sulfurization. Sealed tube anneals were also performed as an alternative to using the tube furnace.	74
5.5 Measured XRD spectrum for CuTaS_3 sample (blue) with CuTaS_3 reference spectrum (red) shown for comparison. The sample was deposited by e-beam (40 nm Ta and 22 nm Cu) and then annealed in a S ambient. .	75
5.6 Measured absorption coefficient (α) for a CuTaS_3 thin-film sample prepared by sulfurization of a Cu-Ta multilayer precursor.	76

LIST OF TABLES

<u>Table</u>	<u>Page</u>
2.1 Ideal metal-semiconductor contact behavior based on relative work-functions.	26
5.1 Comparison of CuTaS ₃ efficiency to leading thin-film solar cell technologies.	72

1. INTRODUCTION

Motivation for solar cell research is straightforward—our sun constantly radiates immense energy which we can harness through photovoltaic energy conversion. The increasing demand for energy and the cost of fossil fuels has brought solar energy to center stage in the last half-century, although the capability of generating electric current using sunlight has been known since the photovoltaic effect was first discovered in 1839. [1] Applications for solar cells at present include both space applications—communications satellites and space exploration—as well as more commonplace functions such as supplementing the electrical grid, powering hand-held calculators, and charging cellular phone batteries. The multitude of possible uses for this technology continues to fuel the development of contending material chemistries used for solar cells.

The purpose of the research presented in this thesis is to prepare semiconducting thin films of novel materials which have been predicted to be effective solar absorbers. Thin-film solar cells exhibit low cost and ease of fabrication compared to those made with bulk single crystals. The highest reported efficiencies for thin-film solar cells are those of CdTe and copper indium gallium selenide (CIGS), at 16.5% and 18.9%, respectively. [2] A material demonstrating competitive efficiency as well as natural abundance and low cost of manufacturing would clearly be of value in the ever-expanding solar energy industry.

In this thesis two potential materials are synthesized and evaluated as thin-film solar absorbers: Cu_3PSe_4 and CuTaS_3 . In addition to the natural abundance of its constituent elements, Cu_3PSe_4 looks promising as a solar absorber since it has a calculated band gap of 1.38 eV, a reasonable mobility ($13\text{-}20\text{ cm}^2\text{V}^{-1}\text{s}^{-1}$), and a calculated absorption coefficient ($\alpha > 1 \times 10^5\text{ cm}^{-1}$ at 1.2 eV above its band gap) comparable to that of CIGS. The technique used for growing such films is pulsed laser deposition (PLD), selected for

its simplicity, rapid throughput, and reputation for preserving the target stoichiometry in resulting films. Electron-beam (e-beam) evaporation was used in addition to PLD for synthesizing CuTaS_3 thin-films.

This thesis is arranged as follows: Chapter 2 provides an introduction to solar cells and their operation, including a discussion on desired absorber material properties. Chapter 3 explains the theory of experimental techniques used for film deposition, modification, and characterization. Chapter 4 contains experimental results for Cu_3PSe_4 , as does Chapter 5 for CuTaS_3 . Lastly, conclusions and recommendations for future work are presented in Chapter 6.

2. LITERATURE REVIEW

This chapter forms the background for research presented in this thesis. An introduction to solar cells is provided for familiarity with device behavior and geometry. A discussion of the current leading thin-film solar cell technologies follows, including cadmium telluride (CdTe), copper indium gallium diselenide (CIGS), and hydrogenated amorphous silicon cells (a-Si:H). The chapter concludes with a summary of the desired traits of an absorber material.

2.1 Introduction to solar cells

Since the materials discussed in this thesis apply specifically to solar cells, it is appropriate to begin with an introduction to solar cells and the photovoltaic effect. This section begins with an overview of crystalline and thin-film solar cell structures, and the purposes of their various layers. The operation of an ideal solar cell is presented, followed by a discussion of deviations from ideal behavior. Device characterization and parameters of interest are then considered. The spectrum of radiation emitted from the sun is introduced, as this energy is absorbed by solar cells and therefore is fundamental to this thesis. This section concludes with a discussion of desired qualities for solar cell absorber layers and the problem of creating ohmic contacts.

2.1.1 Device structure

A simple monocrystalline silicon solar cell structure is shown in Fig. 2.1. The cell is essentially a p-n junction diode with a large surface area onto which photons impinge. [13] The front contact is patterned in a 'finger' structure to allow light to reach the emitter. [4, 13, 14] This contact must be highly conductive and provide satisfactory electrical contact to the emitter. [15] Its work function must be less than that of the n-type emitter

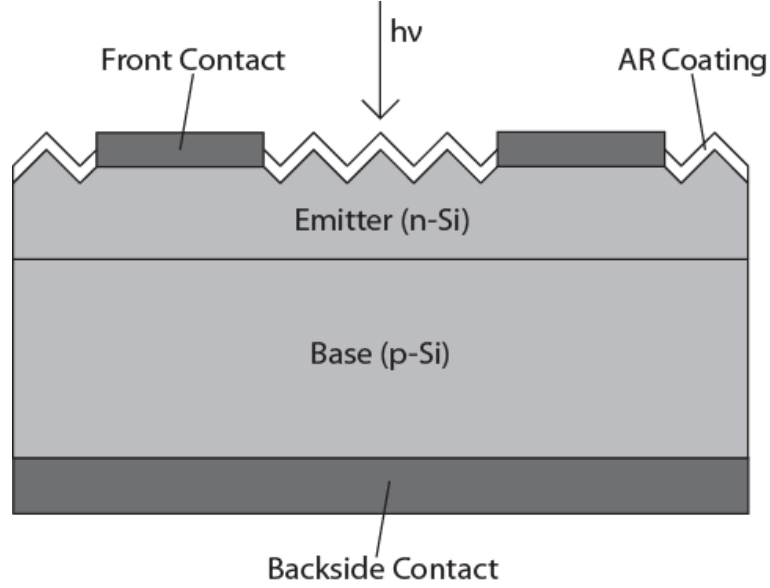


Figure 2.1: Structure of a monocrystalline silicon solar cell.

for ohmic contact. [1, 16] The antireflective (AR) coating and textured surface are used to promote light trapping, in which reflection of light away from the solar cell is reduced. [2, 4, 15]

The reflectance R at an interface between two materials with refractive indices n_1 and n_2 is given by [2, 15, 17]

$$R = \left(\frac{n_1 - n_2}{n_1 + n_2} \right)^2. \quad (2.1)$$

It is evident that a small difference in refractive indices is required to achieve low reflectance. Thus, the large difference between the indices of silicon ($n = 3.4$) and air ($n = 1$) is problematic. An effective AR coating reduces reflectance at both the air-AR and AR-emitter interfaces, and may consist of several layers of gradually increasing refractive indices. [15] The surface texture effectively increases the cell's surface area and improves the total internal reflection of poorly absorbed light reflected back towards the surface. [4, 15]

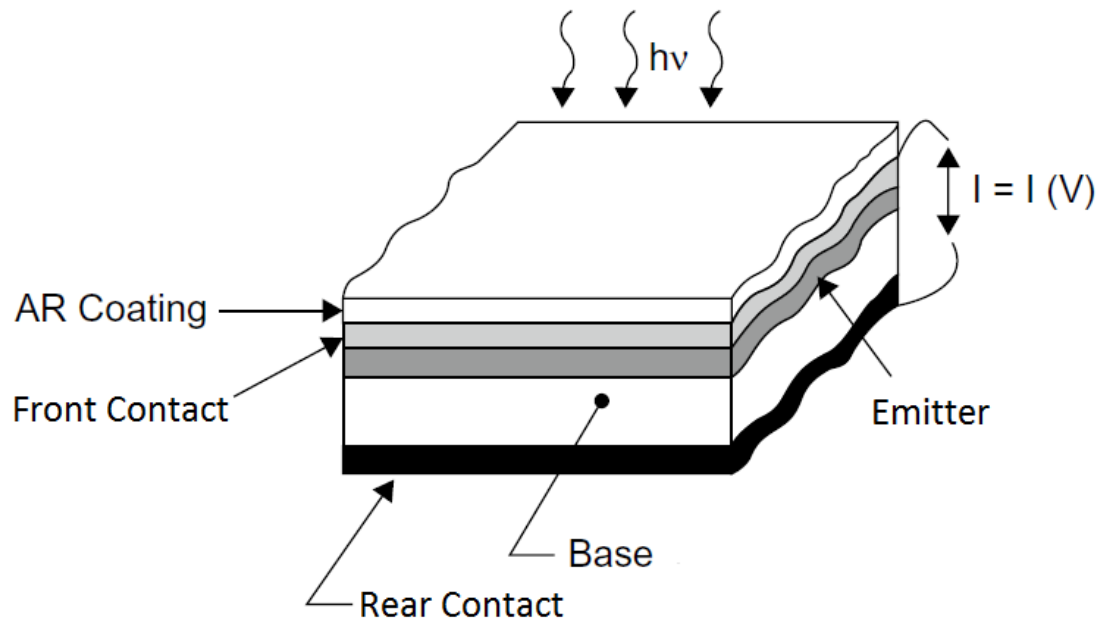


Figure 2.2: Thin-film solar cell stack. [1]

The p-type bulk silicon forms the solar cell's base, or absorber. This bulk is doped by diffusion of phosphorus or another n-type dopant to form the emitter. The emitter-base junction is shallow to allow for high optical transmission to the base, where absorption occurs.

Similar to the front contact, the rear or backside contact must have high conductivity and good electrical contact to the base. Its work function must be higher than that of the p-type base to form an ohmic contact. [1, 16]

Thin-film solar cells provide elaboration on the monocrystalline cell structure. The various device layers are deposited onto a substrate, which is no longer an active layer but simply provides structural stability to the cell. In some cases a superstrate is used in lieu of a substrate and is located on top of the stack rather than the bottom. [4, 15] A superstrate serves as a window layer and must additionally be highly transparent. An example thin-film solar cell stack is shown in Fig. 2.2.

Transparent conducting oxides (TCOs) are often used as top contacts in thin-film solar cells for their high conductivity and transparency. [1] Such contacts may also serve as AR coatings, promoting light trapping with a textured surface and lower index of refraction than the absorber. [15] Light trapping is more important for thin-film solar cells, since the thinner absorber requires light to be reflected several times between the front and back surfaces. A highly reflective backside contact is thus desired to reflect any poorly absorbed light back towards the base. [15]

2.1.2 Ideal solar cell operation

The ideal solar cell is used as a starting point in understanding solar cell device operation. In this model it is assumed that all incident photons with energy $h\nu \geq E_g$ are absorbed, where E_g is the band gap of the cell's absorber layer. The inverse is also assumed: if $h\nu < E_g$ then the photon is not absorbed by the cell. Optical absorption of a photon generates one electron-hole pair by exciting an electron from the absorber's valence band to the conduction band. Energy in excess of E_g is lost in the form of heat as the carrier thermalizes to the conduction band edge. [4, 15, 18]

Figure 2.3 shows the energy band diagram for an unbiased p-n junction like that of a solar cell. Under dark conditions as shown in (a), thermal generation is the only mechanism for minority carrier generation. These carriers are swept across the depletion region by the built-in voltage, V_{bi} , resulting in a small conventional current flowing from emitter to base. This is balanced by an equally small diffusion of majority carriers in the opposite direction, and the net current is zero. Introducing illumination as in (b) provides photogeneration of carriers and a photocurrent I_{ph} from emitter to base. [13] Operation is simplest under short-circuit conditions. Here the total cell current is the short-circuit current I_{sc} and is equal to I_{ph} .

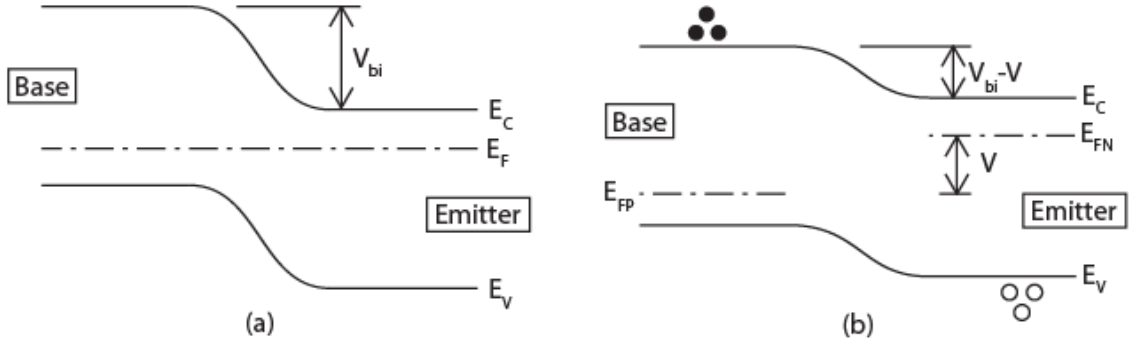


Figure 2.3: Energy band diagrams for a solar cell (a) in the dark, and (b) under illumination.

Under non-short-circuit conditions, a portion of the photogenerated carriers accumulate as minority carriers on either side of the p-n junction depletion layer. This photocarrier-induced effect gives rise to the photovoltage, V , which forward biases the junction. This is indicated in Fig. 2.3 (b). A resulting diffusion current from base to emitter flows when an unilluminated solar cell is biased by a voltage, V . In the context of a solar cell, this gives rise to a dark current I_{dark} , given by [4, 13, 18]

$$I_{dark}(V) = I_s \left(e^{\frac{qV}{k_B T}} - 1 \right), \quad (2.2)$$

where I_s is the reverse saturation current of the diode. When a resistive load, R_L , is connected to an illuminated solar cell, the net current through the load is given by, [2]

$$I = I_{ph} - I_{dark} = I_{ph} - I_s \left(e^{\frac{qV}{k_B T}} - 1 \right). \quad (2.3)$$

Under open-circuit conditions ($I = 0$), I_{dark} and I_{ph} are equal in magnitude and the voltage across the terminals is the open-circuit voltage V_{oc} . It is evident from Eq. 2.3 that an ideal solar cell can be modeled as a current source in parallel with a p-n junction diode, as shown in Fig. 2.4.

The current-voltage characteristics of an ideal cell are shown in Figs. 2.5 and 2.6. The dark cell corresponds to $I_{ph} = 0$ and thus the I-V curve is identical to that of a p-

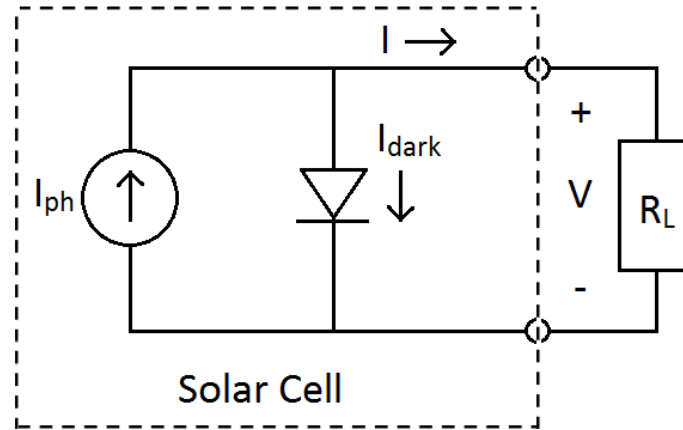


Figure 2.4: Equivalent circuit for an ideal solar cell (within dashed lines) connecting to an external load R_L .

n junction diode. The illuminated I-V curve can be found by shifting the ideal diode curve by I_{ph} on the current axis, in accordance with the superposition principle for solar cells. [2, 4] The load resistance is selected in order to maximize P_{max} and the area of the maximum power rectangle, as shown in Fig. 2.6. P_{max} is less than the $I_{sc}V_{oc}$ product, which is not realizable.

2.1.3 Non-ideal solar cell operation

Understanding the behavior of real solar cells builds on the foundation of the ideal cell. Non-idealities presented in this section include non-radiative recombination, series and shunt resistances, imperfect absorption, and charge extraction difficulties.

Many of the non-idealities presented result from defects in polycrystalline materials. Grain boundaries constitute the most notable defect type. Point defects include self-interstitials, vacancies, antisite defects, and impurities. Self-interstitials and vacancies may be created or annihilated at grain boundaries. Impurities may accumulate at grain boundaries. Some defects introduce electronic energy states which are called 'trap

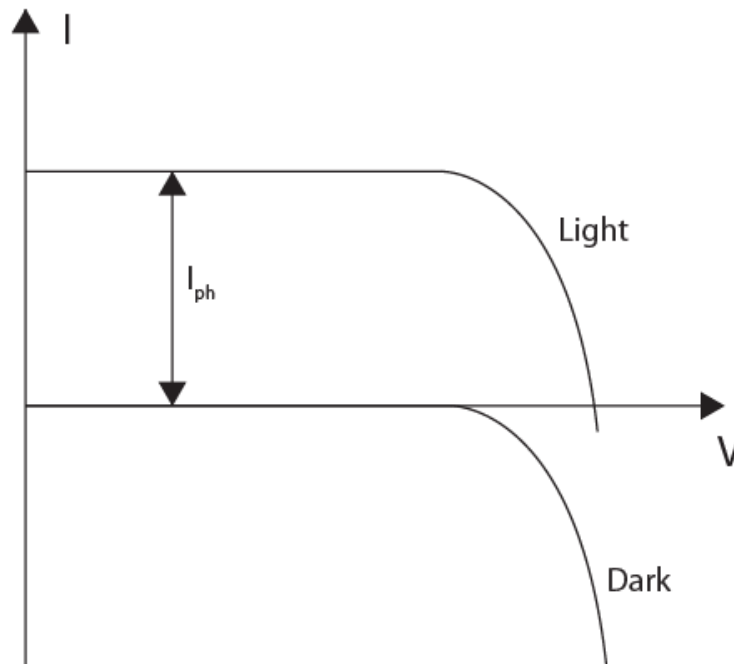


Figure 2.5: Ideal solar cell I-V curves under dark and illuminated conditions.

states' should they fall within the band gap. Trap states tend to facilitate recombination between majority and minority carriers. Charge due to interface states at the grain boundary serves to bend the energy bands, often forming potential barriers to carriers, thereby impeding current flow. Despite these significant effects, a material's band gap and optical absorption are largely unaffected in polycrystals since grain size is relatively large on the quantum-mechanical scale. [4]

Recombination in a non-ideal solar cell differs from that of an ideal device, which is purely radiative (or band-to band) recombination for a direct-bandgap material. In this process, as shown in Fig. 2.7 (a), an electron in the conduction band recombines with a hole in the valence band. The energy $h\nu$ is equal to the band gap of the material and is emitted in the form of a photon of frequency ν . [1, 14]

In actual cells, the non-radiative mechanisms of Auger and Shockley-Read-Hall (SRH) recombination may contribute to establishing the minority carrier lifetime. Figure

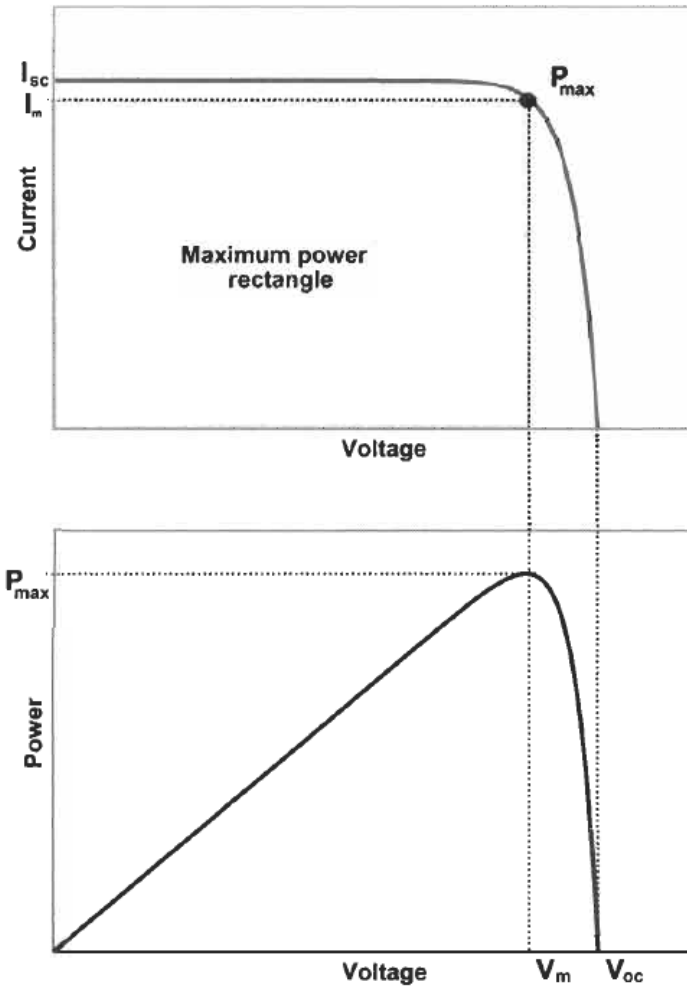


Figure 2.6: Current-voltage (I-V) and power-voltage (P-V) curve for an ideal solar cell.
[2]

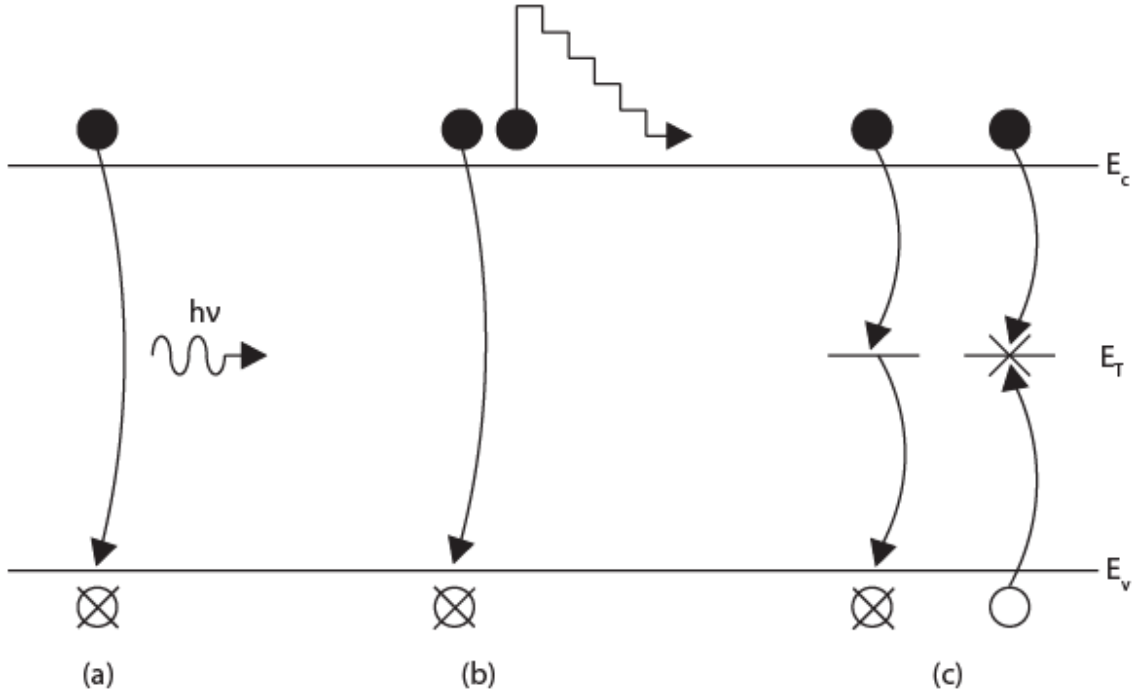


Figure 2.7: Energy band diagrams of (a) radiative, (b) Auger, and (c) Shockley-Read-Hall recombination processes.

2.7 (b) shows Auger recombination, in which the recombination energy due to electron-hole pair annihilation is transferred to another conduction band electron, after which the excited electron thermalizes back to the bottom of the conduction band. The stair-step line in Fig. 2.7 indicates this thermalization process, where the electron emits heat to the lattice via the excitation of phonons. [1, 14, 19, 20, 21]

SRH recombination is illustrated in 2.7 (c). The mid-gap energy state E_T results from defects or impurities in the absorber material. [14] There are two ways to think about SRH recombination: E_T can act as an intermediate state for a conduction band electron as it loses energy and transitions to the valence band in two steps, or recombination may take place at E_T as a valence band hole loses energy and meets a trapped electron. Similar to Auger recombination, the energy emitted from this process is given off as heat. [1, 14]

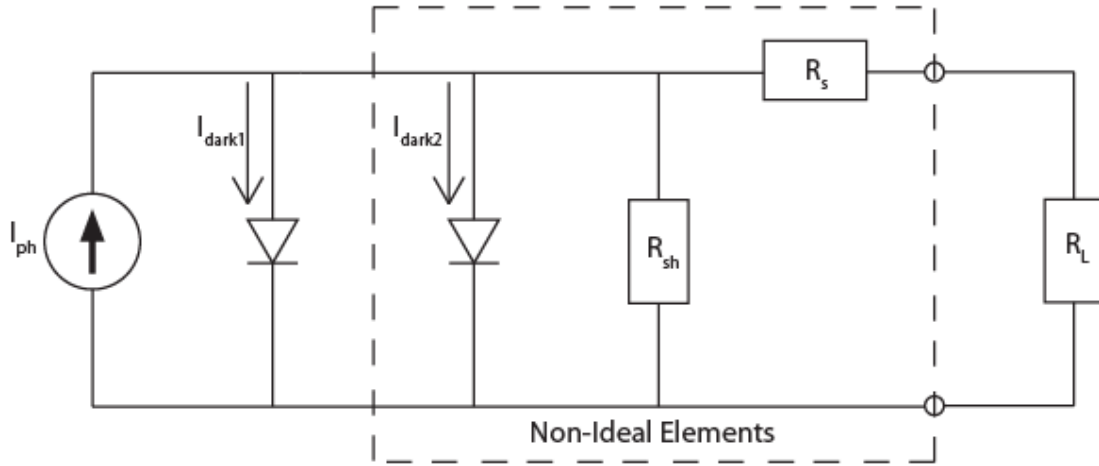


Figure 2.8: Equivalent circuit model for a non-ideal solar cell. Non-ideal elements are contained by the dashed lines.

The effect of these non-radiative mechanisms is an increase in I_{dark} . [2] This is represented in the non-ideal equivalent circuit model as a second diode, as seen in Fig. 2.8. The total dark current is the sum of I_{dark1} from the ideal model and the non-ideal current I_{dark2} , which is introduced to fit observed data. The expression for I_{dark2} employs an ideality factor of 2, and accounts for recombination in the depletion region. [2, 4] The series and shunt resistances in the model, R_s and R_{sh} , serve to distort the current-voltage curves for the solar cell. Contributions to R_s are the resistances from each component of the structure, including the base and emitter regions, front and rear contact interfaces, and the metal contacts themselves. [2, 4] Leakage current in the solar cell results from R_{sh} , which is ideally infinite. [4] The load resistor R_L is external and not part of the solar cell device. Figure 2.9 shows the effects of R_s and R_{sh} on the current-voltage characteristics of the solar cell.

In practice, absorption in the solar cell is not a step function which transitions perfectly from 0 to 100% at E_g . Rather, it continuously increases for materials of finite

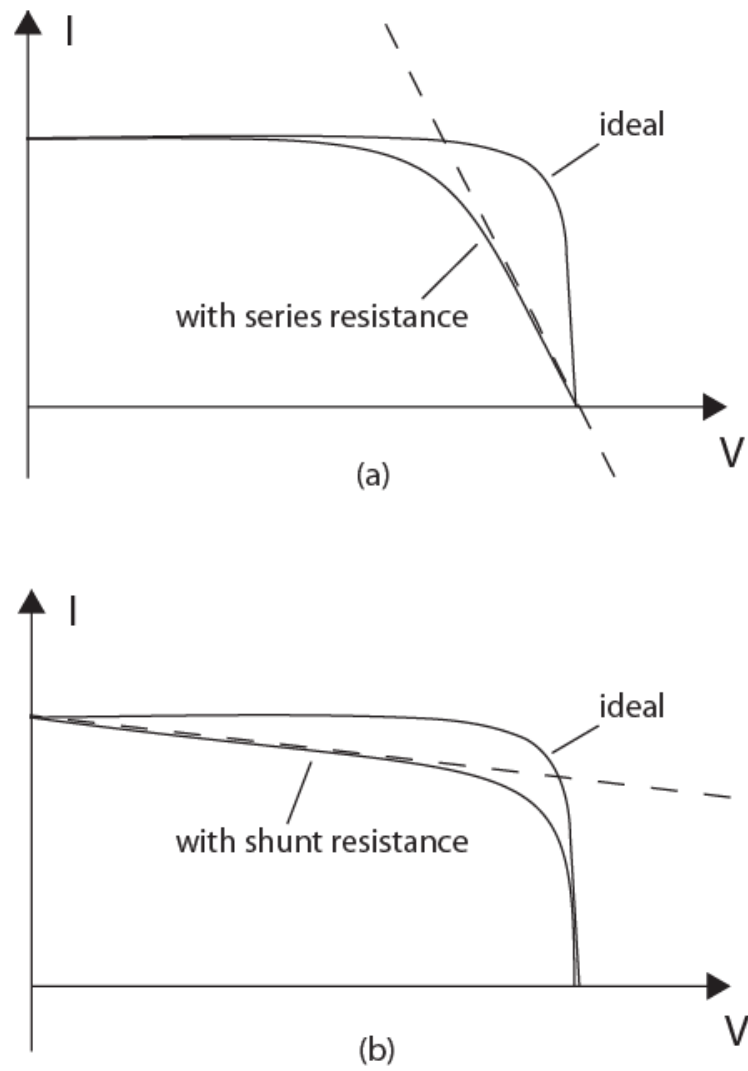


Figure 2.9: Effect of (a) series and (b) shunt resistance on solar cell I-V curves.

thickness. [15] Since not all photons above E_g are absorbed, quantum efficiency in the cell is reduced from its ideal value.

Extraction of photo-generated carriers is critical to solar cell performance. This is affected by carrier lifetime, mobility, and contact selectivity. Insufficient mobility or minority carrier lifetimes will provide for recombination before the carriers may be collected at the device terminals. Mobility is particularly important for thin-film solar cells, in which it is reduced by grain boundaries. [15] An applied voltage cannot be used to improve extraction, since transport of minority carriers to the depletion region is entirely diffusive. Additionally, the diffusion of some minority carriers in the wrong direction (away from the depletion region) results in contact recombination and a decrease in photocurrent. For this reason it is desirable for each contact to present a potential energy barrier to minority carriers, allowing them to diffuse only towards the depletion region.

2.1.4 P-i-n solar cells

Extraction of photocarriers in a material with low carrier mobility is improved by the use of a p-i-n solar cell structure shown in Fig. 2.10. In this configuration, a wide intrinsic (undoped) layer is inserted between the n- and p-regions in the device. [14, 18] The constant electric field spanning the intrinsic region serves as the driving force for the drift of carriers which are either photogenerated in this region or have diffused into it. Electrons and holes are swept towards the n- and p-regions, respectively. This increases the likelihood of successful carrier extraction before recombination may occur. It is evident that the primary transport mechanism in the p-i-n geometry is drift, rather than diffusion as in the p-n structure.

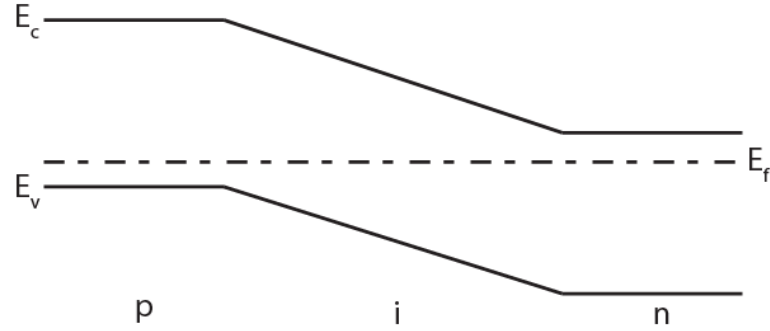


Figure 2.10: Energy band diagram for a p-i-n solar cell.

2.1.5 Multi-junction solar cells

The motivation for multi-junction solar cells lies in the tradeoff between open-circuit voltage and photocurrent. Increasing E_g produces higher V_{oc} , and is therefore desirable. But since only photon energies above the band gap are absorbed, increasing E_g also reduces the useable amount of the solar spectrum and in turn produces lower I_{ph} . From this tradeoff it is evident that high I_{ph} and V_{oc} are not simultaneously realizable with only one band gap in the device.

One solution to increase efficiency is the multi-junction solar cell. Both tandem (two-junction) and triple-junction devices are popular. [3, 18] As shown in Fig. 2.11, each junction targets photons of different energies for absorption by employing a different band gap. [3] The bottom absorber ensures absorption of low energy photons which are not typically absorbed in single-junction devices. Middle and top absorbers improve the efficiency of absorption by minimizing the energy emitted as heat as higher-energy photocarriers thermalize to the band edges. In this fashion, multi-junction solar cells make better use of the solar spectrum. [3, 15]

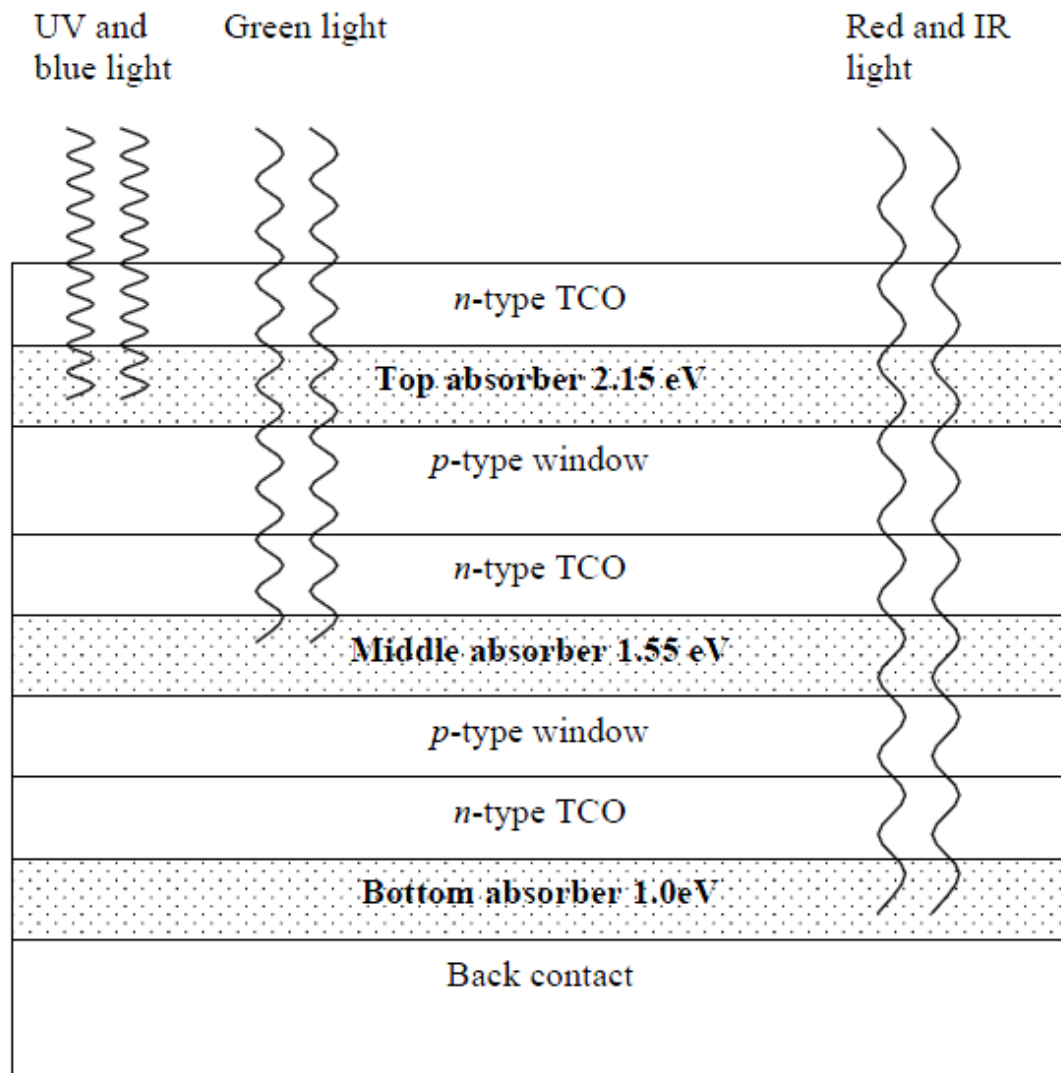


Figure 2.11: Triple-junction solar cell structure. [3]

2.1.6 Device characterization

Solar cell performance is evaluated by inspecting the current-voltage characteristics of the illuminated cell. The four quantities of primary importance are the short-circuit current (I_{sc}), open-circuit voltage (V_{oc}), fill factor (FF), and cell efficiency (η). [4, 22] In this section, these parameters are introduced and discussed in the context of both an ideal and non-ideal solar cell.

I_{sc} is the current which flows through the terminals of the solar cell under short-circuit conditions. [1, 4] A large short-circuit current corresponds to efficient photocarrier generation and extraction, and is desired in order to transport as many photocarriers to the load as possible. I_{sc} is a function of the incident radiation intensity and the solar cell quantum efficiency.

V_{oc} is the voltage across the solar cell terminals under open-circuit conditions. A large V_{oc} value indicates a small dark current in the cell, which is desired to maximize the number of photocarriers reaching the load. Since V_{oc} increases with band gap, an excessively large V_{oc} may be undesirable since less of the solar spectrum is utilized for photogeneration with increasing E_g .

Expressions for I_{sc} and V_{oc} are straightforwardly obtained in the ideal solar cell model. Figure 2.12 shows the ideal solar cell equivalent circuit under (a) short-circuit, and (b) open-circuit conditions. Current through the device terminals, I , is given by the Shockley solar cell equation [2],

$$I = I_{ph} - I_s \left(e^{\frac{qV}{k_B T}} - 1 \right), \quad (2.4)$$

where V is the voltage across the device terminals, and I_s is the diode's reverse saturation current. Under short-circuit conditions, $V = 0$ and I is the short-circuit current. Here Eq. 2.4 simplifies to [2]

$$I = I_{sc} = I_{ph}. \quad (2.5)$$

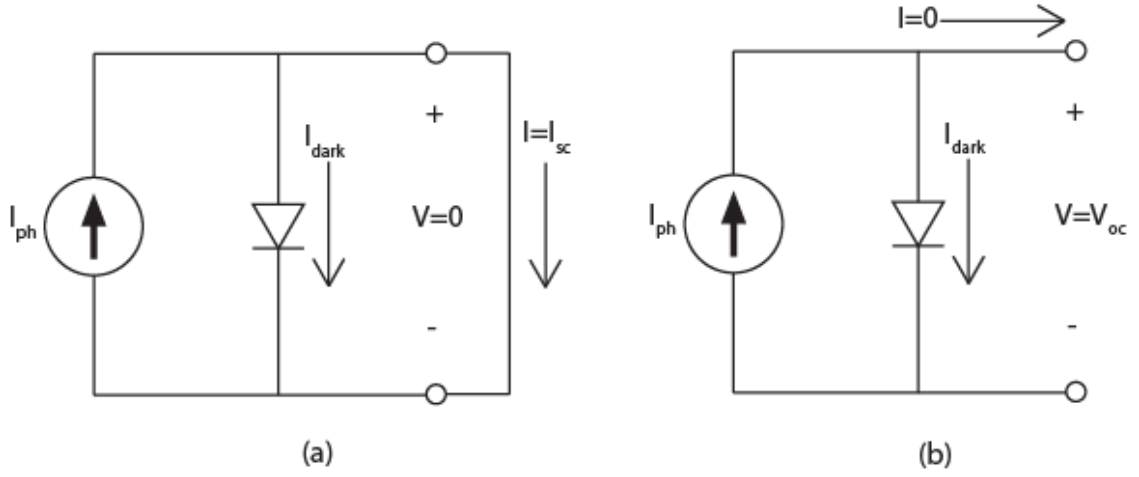


Figure 2.12: Ideal solar cell equivalent circuit under (a) short-circuit, and (b) open-circuit conditions.

Under open-circuit conditions, $I = 0$ and V is the open-circuit voltage. Equation 2.4 then becomes [2, 4, 18]

$$I = I_{ph} - I_s \left(e^{\frac{qV_{oc}}{k_B T}} - 1 \right) = 0. \quad (2.6)$$

Solving for V_{oc} yields [2]

$$V_{oc} = \frac{k_B T}{q} \ln \left(\frac{I_{ph}}{I_s} + 1 \right). \quad (2.7)$$

From Eq. 2.7 it is evident that a large photocurrent and low reverse saturation current are desired to achieve a large V_{oc} .

The short-circuit current and open-circuit voltage decrease from their ideal values in the non-ideal solar cell model. Figure 2.13 shows the non-ideal solar cell equivalent circuit under (a) short-circuit, and (b) open-circuit conditions. The dark current now includes I_{dark2} to account for recombination in the depletion region, with ideality factor 2. Applying Kirchhoff's current law to the circuit in Fig. 2.13 (a) provides the equation,

$$I_{ph} = I_{dark1} + I_{dark2} + I_{sh} + I_{sc}. \quad (2.8)$$

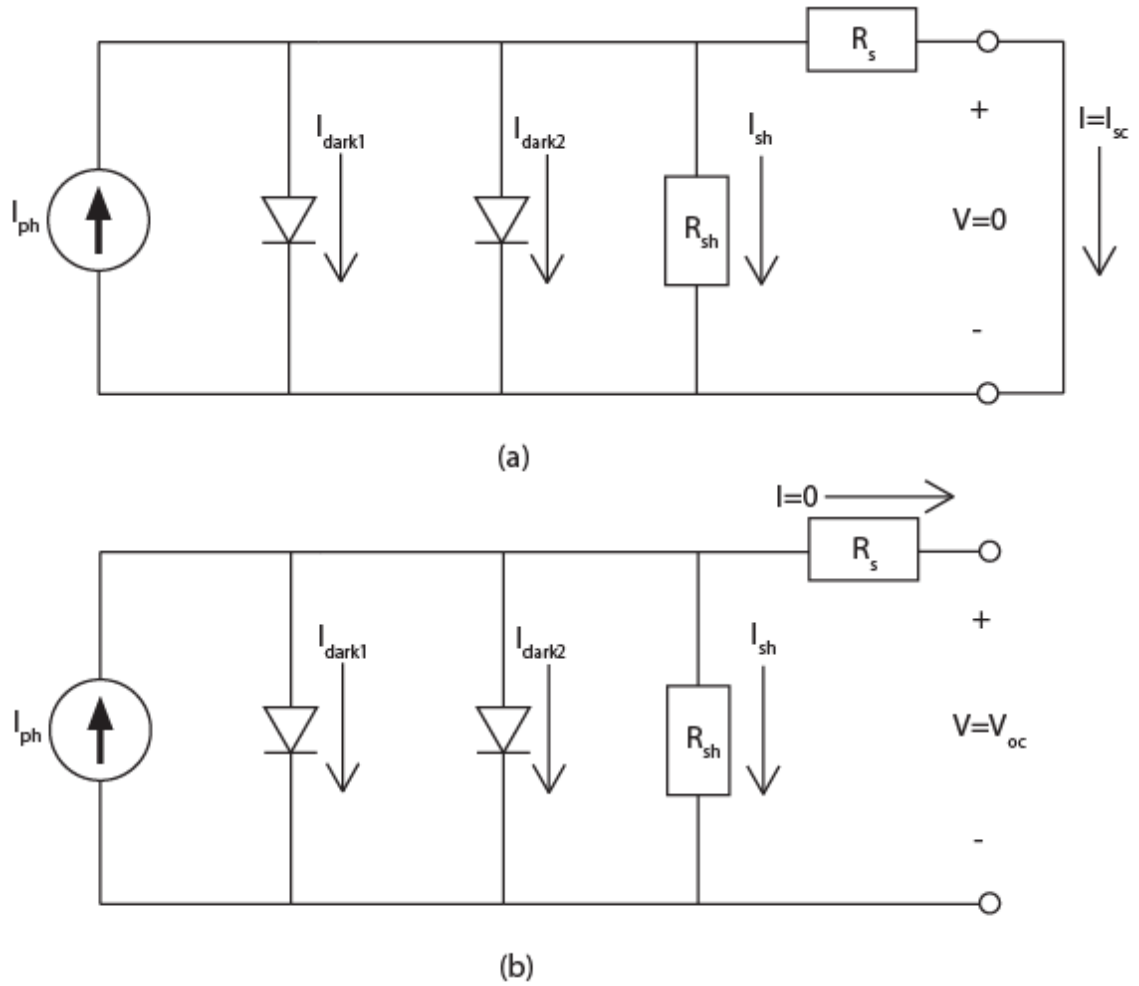


Figure 2.13: Non-ideal solar cell equivalent circuit under (a) short-circuit, and (b) open-circuit conditions.

Solving for the short-circuit current yields [2]

$$\begin{aligned} I_{sc} &= I_{ph} - I_{dark1} + I_{dark2} + I_{sh} \\ &= I_{ph} - \left[I_{s1} \left(e^{\frac{q(V+I_{sc}R_s)}{K_B T}} - 1 \right) + I_{s2} \left(e^{\frac{q(V+I_{sc}R_s)}{2K_B T}} - 1 \right) + \frac{V + I_{sc}R_s}{R_{sh}} \right]. \end{aligned} \quad (2.9)$$

Here the expression $V + I_{sc}R_s$ is the voltage across the diodes and R_{sh} . Comparing Eqs. 2.5 and 2.9 shows that the quantity within the brackets is the difference in short-circuit current between the ideal and non-ideal models. Thus, a solar cell's short-circuit current is reduced by the non-ideal effects of dark current, shunt conductance, and parallel resistance.

Open-circuit voltage also decreases from non-ideal effects. Applying Kirchhoff's current law to the circuit in Fig. 2.13 (b) gives the equation

$$I_{ph} = I_{dark1} + I_{dark2} + I_{sh}. \quad (2.10)$$

Since $I = 0$, the V_{oc} is the voltage across both diodes and R_{sh} . Equation 2.10 then becomes

$$I_{ph} = I_{s1} \left(e^{\frac{qV_{oc}}{K_B T}} - 1 \right) + I_{s2} \left(e^{\frac{qV_{oc}}{2K_B T}} - 1 \right) + V_{oc} G_{sh}, \quad (2.11)$$

where G_{sh} is the shunt conductance (ideally $G_{sh} = 0$). This can be rearranged as

$$V_{oc} = \frac{1}{G_{sh}} \left[I_{ph} - I_{s1} \left(e^{\frac{qV_{oc}}{K_B T}} - 1 \right) - I_{s2} \left(e^{\frac{qV_{oc}}{2K_B T}} - 1 \right) \right]. \quad (2.12)$$

From this expression it is evident that a solar cell's open-circuit voltage decreases from the non-ideal effects of shunt conductance and dark currents.

Since I_{sc} and V_{oc} are clearly not simultaneously realizable, the power delivered to the external circuit (P_{out}) is less than their product. P_{out} is dependent on the load impedance, which is selected to maximize the $I \times V$ product. Figure 2.6 shows a plot of photocurrent density vs. bias voltage, with V_m and I_m corresponding to the voltage and current achieved when the load is selected to provide maximum power.

The fill factor is the ratio of this maximum power density to the $I_{sc} \times V_{oc}$ product, given by [1, 2, 3, 4, 13, 15, 18, 22]

$$FF = \frac{V_m J_m}{J_{sc} V_{oc}}. \quad (2.13)$$

By definition, $FF \leq 1$ with $FF = 1$ corresponding to a perfectly rectangular I-V curve where $I_m = I_{sc}$ and $V_m = V_{oc}$. The fill factor is a measure of how well the actual I-V curve resembles this rectangular shape. [1] In actual solar cells, fill factors of around 0.8 are achievable. [13, 18] Non-ideal resistances R_{sh} and R_s serve to lower V_m and I_m from V_{oc} and I_{sc} , respectively, and in turn decrease FF. The fill factor of a non-ideal solar cell is given by [2]

$$FF \approx FF_0 \left(1 - \frac{R_s I_{sc}}{V_{oc}}\right), \quad (2.14)$$

where FF_0 is the fill factor of an ideal solar cell.

Solar cell efficiency, η , is then a ratio of the maximum power to the illumination power incident on the cell, P_s [1, 4, 18, 21, 22]:

$$\eta = \frac{V_m I_m}{P_s} = \frac{I_{sc} V_{oc} FF}{P_s} \quad (2.15)$$

The task of maximizing η involves tuning E_g to the solar spectrum, as discussed in Section 2.1.7. From Eq. 2.15 it is apparent that reductions in short-circuit current, open-circuit voltage, and fill factor will have detrimental effects on η .

2.1.7 Solar spectrum radiation

The electromagnetic energy provided by the sun, called the solar spectrum, spans a range of wavelength from 0.2 to 3.0 μm . [13] Since optical absorption occurs as light passes through air, the solar intensity is greatest (140 mW/cm^2) outside the atmosphere. Figure 2.14 shows the corresponding spectrum, called air-mass-zero or AM0. Light which travels through the atmosphere along the shortest possible path to the earth's surface, when the sun is directly overhead, is called AM1. Light traveling along twice that

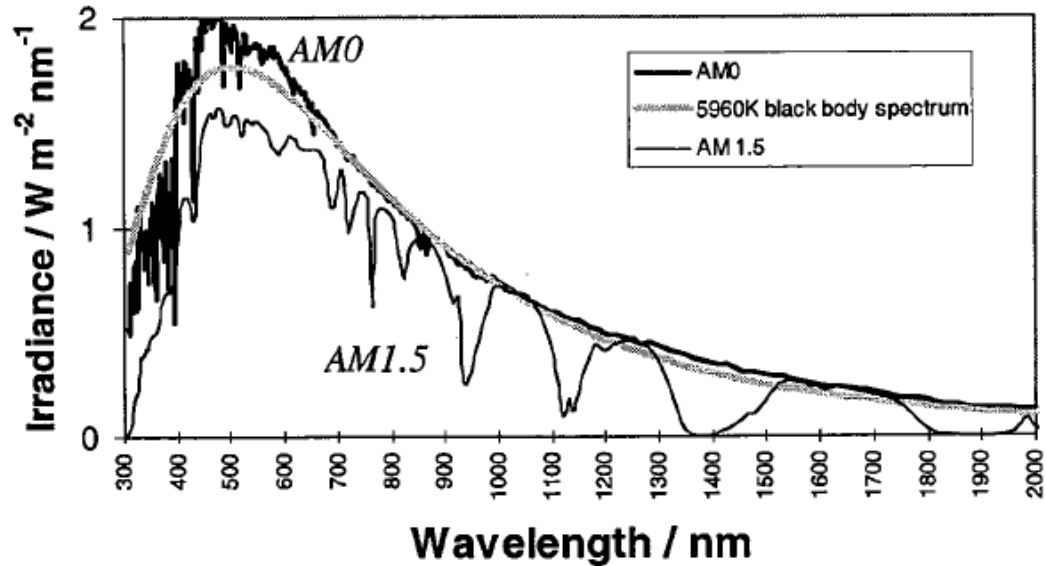


Figure 2.14: AM0 and AM1.5 solar spectra. [4]

path length is AM2. The AM1.5 spectrum, equivalent of the sun at a 42° angle of elevation and an intensity of 1000 W/m^2 , is the standard used for photovoltaic characterization. [4]

The solar spectrum is of paramount importance in the design of solar cells, since the energies of photons used for photovoltaic energy conversion are within this spectrum. The band gap of an absorber material must be less than the energy of an incident photon ($h\nu \geq E_g$) in order for photon absorption to occur. Thus, a large E_g yields a small photocurrent. However, the band gap should not be too small since the V_{oc} of the cell may not exceed E_g . Therefore, an optimal band gap exists for any radiation spectrum. Figure 2.15 shows the efficiency of a cell as a function of E_g for the AM1.5 spectrum.

2.1.8 Ohmic contact theory and formation

A significant difficulty in solar cell fabrication lies in achieving an ohmic back contact to the absorber layer. Ohmic contacts are desired for extraction of majority carriers from the device with near-linear current-voltage characteristics and low series resistance.

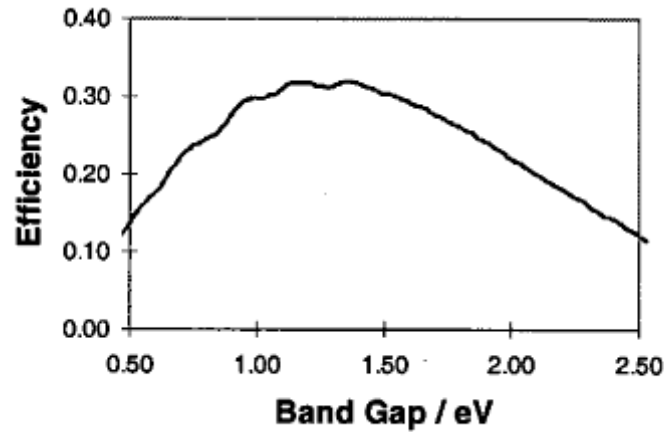


Figure 2.15: Solar cell efficiency vs. band gap for the AM1.5 spectrum. [4]

[23] This section summarizes relevant details of metal-semiconductor contacts and solutions to achieving ohmic behavior.

Figure 2.16 shows the energy band diagrams of a metal and p-type semiconductor before being joined together. The relative band positions are specific to the particular materials used. E_{VAC} is the vacuum level energy, corresponding to the energy of a carrier just outside the material. [18] It follows that the electron affinity, $q\chi$, is the energy required to remove a conduction band electron at E_C from the semiconductor. Similarly, the work-function of a material ($q\phi_M$ for a metal and $q\phi_S$ for a semiconductor) is the energy required to move an electron from the Fermi level to the vacuum level. [8, 24]

Note that the situation shown in Fig. 2.16 involves a metal with a greater work-function than that of the semiconductor. Ideally, this condition allows for the formation of an ohmic contact as the metal is joined with a p-type semiconductor as shown in Fig. 2.17. Electrons flow from the semiconductor into the metal when the two materials are joined, creating a positively charged depletion region near the semiconductor surface. [8] Band bending occurs in the depletion region such that E_{FS} aligns with E_{FM} and equilibrium is achieved. The energy bands in the semiconductor bulk region (far from the interface)

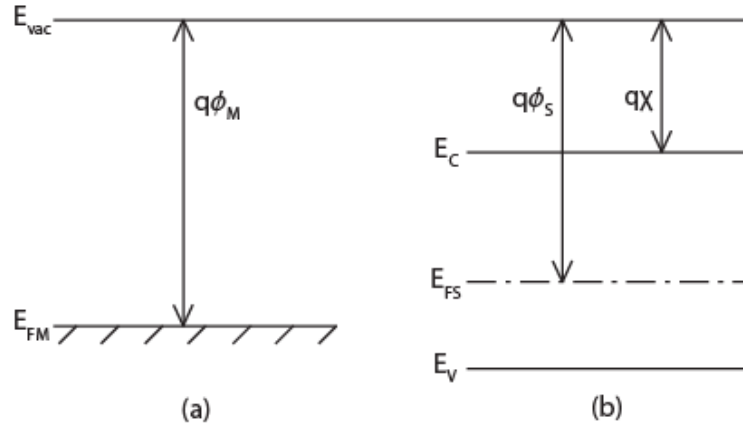


Figure 2.16: Energy band diagrams for (a) metal, and (b) p-type semiconductor materials before being joined together.

are unaffected and remain flat. Bending also occurs in the vacuum level to preserve a constant electron affinity throughout the semiconductor. This results in formation of the local vacuum level, E_{LVAC} . The magnitude of the band bending is the difference in work functions, given by

$$q\phi_{bi} = q(\phi_M - \phi_S), \quad (2.16)$$

where ϕ_{bi} is the junction's built-in voltage. [18] Conduction band electrons migrating from semiconductor to metal must surmount the potential barrier of height $q\phi_{bi}$, and those crossing the interface in the opposite direction observe a greater barrier height of magnitude

$$q\phi_{bn} = q(\phi_M - \chi). \quad (2.17)$$

The carriers of particular interest—majority carrier holes—observe no energy barrier crossing from semiconductor to metal. This situation is desired in solar cells to achieve contact selectivity—extraction of photo-generated holes at the backside contact while preventing electron extraction.

A metal with a work-function lower than that of the semiconductor will ideally form a rectifying contact with a p-type material as shown in Fig. 2.18. [18] This structure

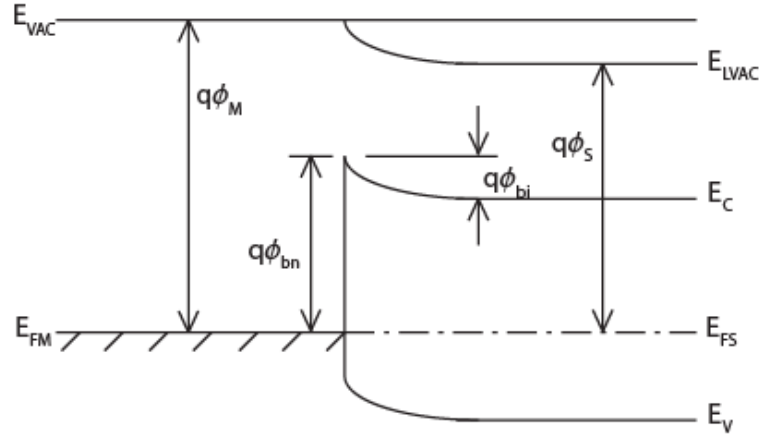


Figure 2.17: Energy band diagram for an ideal ohmic contact formed with a p-type semiconductor.

is known as a *Schottky barrier*, with the semiconductor bands bending to form a barrier to majority carrier conduction. The magnitude of this barrier is again given by the difference in work-functions,

$$q\phi_{bi} = q(\phi_s - \phi_M). \quad (2.18)$$

The primary transport mechanism for current across the junction is thermionic-emission, in which electrons must have kinetic energy of at least $q\phi_{bp}$ to traverse the barrier.[18] It is apparent that this rectifying contact is detrimental to solar cell operation, since the potential energy barrier hinders hole transport from the semiconductor to the metal. [25] It follows that high work-function metals are desired for backside contact materials to prevent Schottky barrier formation.

The preceding discussion of metal-semiconductor interfaces provides a general understanding of device behavior based on the work-functions of the two materials. Table 2.1 shows the resulting contact behavior from each combination of majority carrier type and relative work-functions. This relationship may be used as a rule-of-thumb to select appropriate materials for the desired behavior. In practice, deviations from this generalization exist in the forms of Fermi level pinning and quantum-mechanical tunneling.

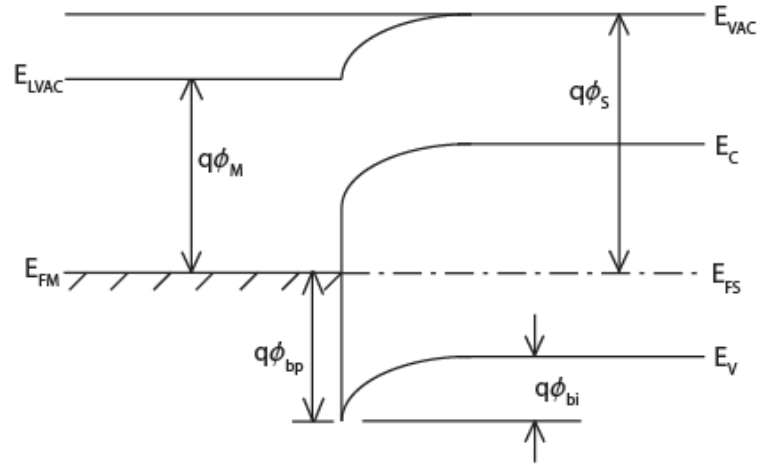


Figure 2.18: Energy band diagram for an ideal rectifying contact formed with a p-type semiconductor.

	p-type	n-type
$\phi_M > \phi_S$	Ohmic	Rectifying
$\phi_M < \phi_S$	Rectifying	Ohmic

Table 2.1: Ideal metal-semiconductor contact behavior based on relative work-functions.

For covalent semiconductors such as Si, Ge, and GaAs, Fermi level pinning results in the formation of Schottky barriers regardless of metal work-function. Values of $q\phi_b$ are typically about $2E_G/3$ and $E_G/3$ for n- and p-type semiconductors, respectively. [8, 23] This phenomenon is a result of dangling bonds on the surface of the semiconductor, which provide surface states within the band gap of the material. An important parameter relating to these surface states is the charge neutral level, located at $E_V + q\phi_0$. States below this level are donor-like (neutral when filled and positively charged when empty), and states above are acceptor-like (negatively charged when filled and neutral when empty). Equilibrium is achieved when electrons flow from the region of the semiconductor near the surface to fill surface states, causing the energy bands to bend upwards until the Fermi level is flat throughout the entire material as shown in Fig. 2.19. These electrons leave behind a depletion region of positive space charge with magnitude Q_{sc} . The total surface state charge, Q_{ss} , is comprised of all filled surface states above the neutral level. The thin interfacial oxide on the semiconductor surface is of thickness δ ($\sim 5\text{--}20$ Å) with a potential Δ across it. [8, 18] This layer is thin enough to be transparent to carrier transport. When the semiconductor is joined with a metal, a negative charge Q_M accumulates on the surface of the metal to balance the surface and space charge.

Fermi level pinning is detrimental to solar cell technologies as ohmic contact formation is prevented. One strategy to mitigate this problem is doping the semiconductor to promote tunneling through the barrier.

Ohmic conduction may be achieved in Schottky barriers if the potential barrier is narrow enough, via quantum-mechanical tunneling as shown in Fig. 2.20. [1, 2, 18] If the barrier is very thin at the valence band, holes tunnel directly as field emission (FE) current (Fig. 2.20 (a)). For thicker barriers, carriers may require some kinetic energy to reach a part of the barrier which is narrow enough to tunnel through. This is called thermionic-field emission (TFE), or phonon-assisted tunneling (Fig. 2.20 (b)). As previ-

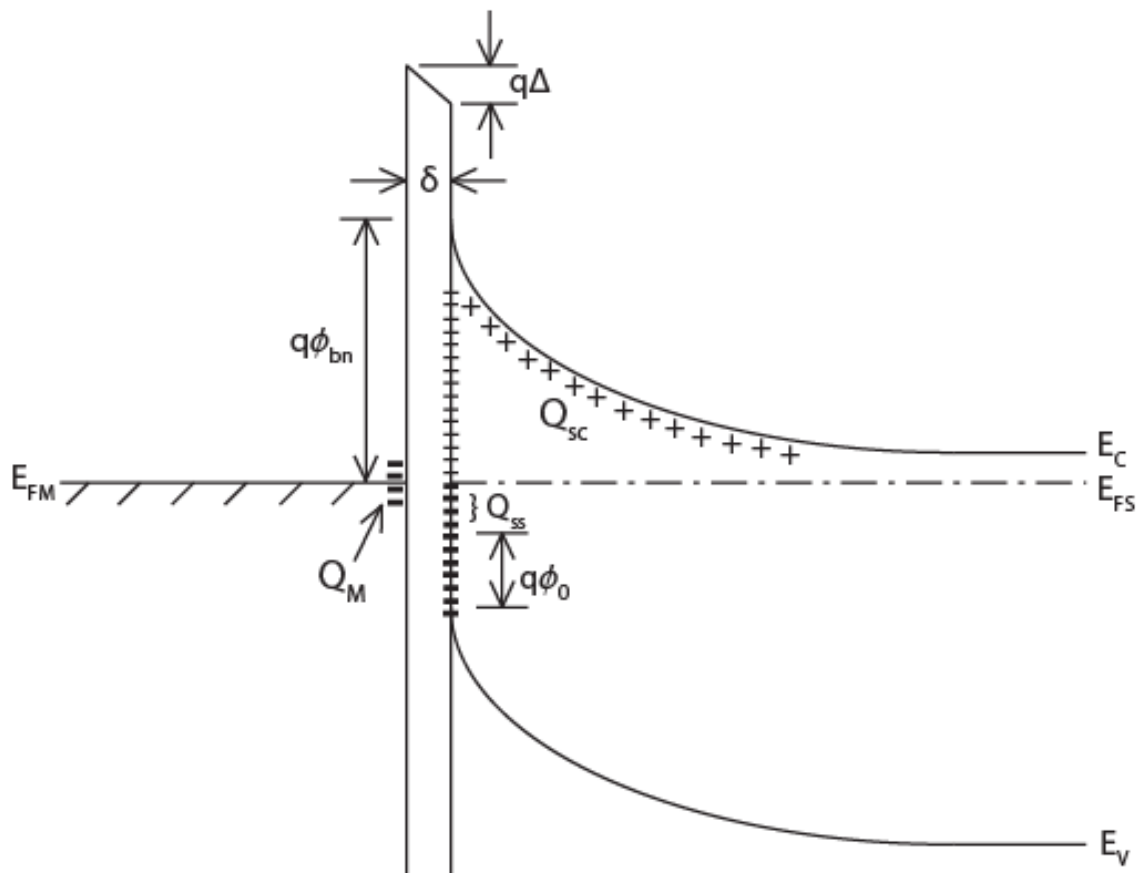


Figure 2.19: Energy band diagram showing Schottky barrier formation from the presence of surface states on an n-type semiconductor.

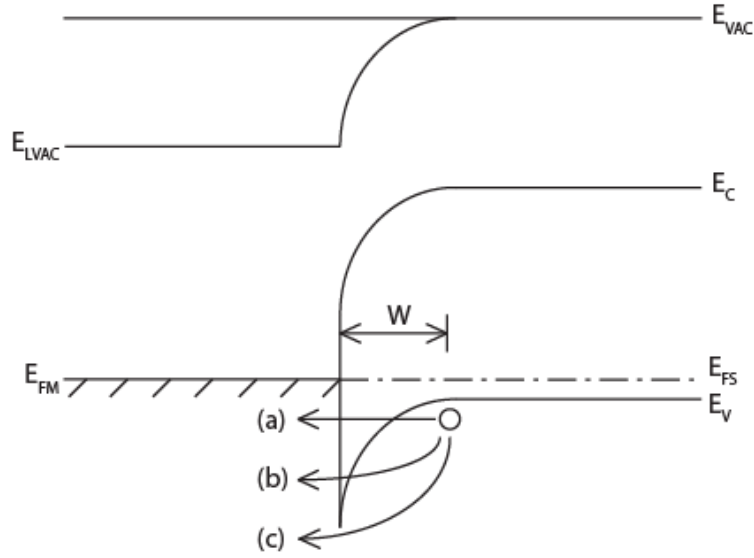


Figure 2.20: Energy band diagram showing (a) field emission, (b) thermionic-field emission, and (c) thermionic emission across a Schottky barrier formed with a p-type semiconductor.

ously described, when no tunneling occurs transport is entirely comprised of thermionic emission current (Fig. 2.20 (c)). The width of the depletion region decreases with doping concentration and is given by [18]

$$W = \sqrt{\frac{2\epsilon_s}{qN} \left(V_{bi} - V_A - \frac{k_B T}{q} \right)}, \quad (2.19)$$

where ϵ_s is the permittivity of the semiconductor, N is the doping concentration, and V_A is the applied voltage. Accordingly, tunneling current increases with doping level and is the transport mechanism responsible for most ohmic contacts on degenerately doped semiconductors. [18] In some cases the semiconductor is degenerately doped only near the surface in order to achieve high field emission current while maintaining lower bulk doping levels. [8, 18, 23] This strategy is useful for solar cell technologies where Schottky barrier formation is unavoidable.

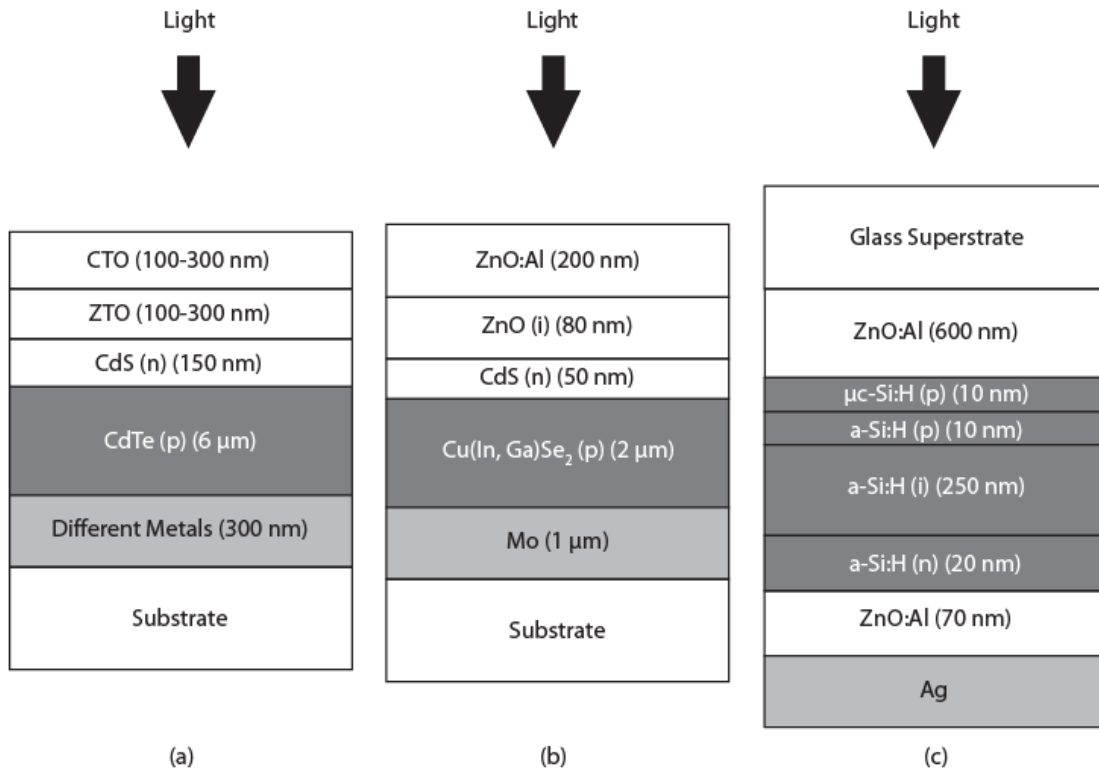


Figure 2.21: Solar cell stacks for (a) CdTe, (b) CIGS, and (c) a-Si:H.

2.2 Thin-film solar cell materials

Crystalline silicon (c-Si) currently accounts for 90% of the world's photovoltaic market, boasting high performance, stability, abundance, and nontoxicity. [22, 26] Although efficiencies of c-Si solar cells (about 25%) are approaching the theoretical maximum efficiency (known as the *Shockley-Queisser limit* or *detailed balance limit*) of $\sim 33.7\%$ and are currently the highest of all photovoltaic technologies, thin-film solutions are thought capable of achieving higher performance. [3, 21, 27, 28] This section is a survey of the three main thin-film photovoltaic materials: amorphous silicon (a-Si), cadmium telluride (CdTe), and copper indium gallium diselenide (Cu(In,Ga)Se₂, or CIGS). [1, 15, 22, 26] Figure 2.21 shows examples of thin-film solar cell configurations employing each of these absorber materials.

2.2.1 Cadmium telluride (CdTe)

The highest efficiencies achieved in CdTe-based solar cells are about 16.5%, as first synthesized in 2001. [29] The band gap is near optimum for PV application, with reported values ranging from 1.44–1.56 eV. [3, 25, 26, 29] CdTe is also extremely absorbing; a mere 1 μm -thick absorber layer is comparable to 200 μm of crystalline Si. Additionally, Cd is highly abundant as a byproduct of zinc production. [26] These qualities plus its ease of production by thermal evaporation has led CdTe to be the most successful thin-film PV technology. [3, 15] Figure 2.21 (a) shows an example CdTe solar cell structure.

Various materials have been used as front contacts in CdTe solar cells, including ITO, $\text{SnO}_2\text{:F}$, $\text{In}_2\text{O}_3\text{:F}$, SnO_2 , and ZnO. [15, 26] The cadmium stannate (Cd_2SnO_4 or CTO) and zinc stannate (Zn_2SnO_4 or ZTO) pairing shown in Fig. 2.21 (a) was developed to replace SnO window layers, contributing to the first 16.5% efficiency cell. [29] CTO films achieved lower sheet resistance, absorption, and roughness than SnO_2 . These cells showed improvements in short-circuit current, fill factor, and efficiency from previous cells. Cadmium sulfide (CdS) is a common buffer layer in solar cells, used as a diffusion barrier between the absorber and front contact. [3, 26]

Downsides of CdTe technology include the toxic nature of Cd and the difficulty in achieving an ohmic backside contact. [3, 15, 25, 26] Conduction is often achieved by carriers tunneling through the potential barrier at the back contact interface. Common contact materials are copper-based metals such as Cu_2Te , ZnTe:Cu , and HgTe:Cu . The diffusion of Cu from these metals into the absorber is problematic, presenting additional stability issues. [26]

2.2.2 Copper indium gallium diselenide (CIGS)

CIGS is currently the most efficient thin-film PV technology, with efficiencies of up to 20%. [3, 15, 26] Development of CIGS began with the first chalcopyrite solar cells,

which used a CuInSe_2 absorber layer with a band gap of about 1.0 eV. By alloying this material with CuGaSe_2 ($E_g = 1.7$ eV) and varying the ratio of gallium to indium, the band gap can be tuned between 1.0 and 1.7 eV. CIGS solar cell absorbers employ a Ga:In ratio of 1:4 and have a band gap of 1.15 eV. [3, 15, 26] An example CIGS solar cell configuration is shown in Fig. 2.21 (b).

Depositing ZnO:Al directly on the CdS layer results in local defects and modification to the band gap. Intrinsic zinc oxide (i- ZnO) is used as an intermediate layer and is important to device performance. [15, 26] As in CdTe devices, cadmium sulfide is used as a buffer layer in CIGS solar cells.

Sputtered molybdenum (Mo) metal is the most common back contact in CIGS solar cells, used for its high work function to form an ohmic contact to the absorber. [15, 26] Other metals such as tungsten, tantalum, and niobium have been explored as alternatives to Mo, which exhibits problematic corrosion and poor optical reflection. [26]

Current problems for CIGS technology are raw materials cost and large area scale-up. [3] Deposition of the CIGS layer uses four-target evaporation methods, which is difficult to employ on large substrates while maintaining device efficiency.

2.2.3 Hydrogenated amorphous silicon (a-Si:H)

Amorphous silicon boasts an absorption coefficient in the visible spectrum almost 100 times higher than that of crystalline silicon (c-Si), and actual a-Si cells are 1000 times thinner than c-Si cells. [26] A large defect density is present in a-Si due to dangling bonds which create energy states deep in the band gap. Hydrogen is introduced to passivate these dangling bonds, forming hydrogenated a-Si (a-Si:H). Despite this passivation, the relatively high defect density results in a low diffusion length of 100–300 nm. For this reason, the p-i-n configuration as shown in Fig. 2.21 (c) is used in a-Si:H solar cells.

[15, 26] The intrinsic a-Si:H layer is much thicker than the doped p- and n-regions for its higher diffusion length.

a-Si shares the benefit of silicon abundance with c-Si. Film growth by plasma-enhanced chemical vapor deposition allows for ease of large area scale-up. [26] Additionally, low process temperatures (100–400 °C) allow the use of many different substrates. Efficiencies of a-Si:H solar cells currently exceed 15%.

One drawback of a-Si is its slightly larger-than-optimal band gap (1.7 eV). A solution to this problem is the layer of hydrogenated microcrystalline silicon (μ C-Si:H) as shown in Fig. 2.21 (c). The band gap of μ C-Si:H is close to the 1.12 eV of c-Si, and is used to absorb lower energy photons. [15]

a-Si suffers from the well-documented Staebler-Wronski effect. [2, 3, 15, 26] This is the illumination-induced degradation of conductivity and absorption, resulting in a 15–30% decrease in performance. The accepted mechanism is an increase in the number of dangling bonds resulting from illumination. Interestingly, these defects are metastable and are repaired by annealing the material at temperatures of 150 °C. This degradation is a major unsolved issue in a-Si:H solar cells. As a result, device structure and properties must be optimized for operation in the degraded state. Thinner absorber layers may be used to reduce the effect, but also detrimentally affect absorption. Thus, light trapping and multi-junction geometries are especially important for a-Si:H solar cells.

2.3 Conclusion

By introducing the structure and operation of thin-film solar cells, this chapter provides a bridge between absorber layer characteristics and overall operation of the complete cell. It is appropriate to conclude with a summary of the most important absorber parameters, which are discussed within the context of the two primary goals of a photovoltaic device [27]:

1. the effective absorption of sunlight for photocarrier generation, and
2. extraction of these photocarriers before they recombine.

For a material to be considered as a potential solar absorber it is preferred to be natively p-type or p-type dopable. This is because solar cells are *bipolar* devices. That is, their operation is determined primarily by minority carrier behavior. Since electrons have higher mobilities than holes, they are the preferred minority carrier. [30] It is also desirable for the material to accept both p- and n-type dopants for homojunction formation. Additionally, p-i-n devices may then be formed by leaving an intrinsic (undoped) region between either doped regions. As discussed above, this is advantageous for charge extraction by introducing drift as a driving force for photocarrier transport.

To effectively absorb sunlight, an absorber should have a direct bandgap which is well suited for the solar radiation spectrum. The optimal bandgap is 1.34 eV, although values within the range of $\sim 1\text{--}1.6$ eV are typically acceptable. [26, 27, 28, 30] An excessively high bandgap detrimentally reduces the usable portion of the solar spectrum (resulting in a low short-circuit current). Too low of a bandgap limits the open-circuit voltage. [3]

The absorption coefficient (α) for absorbers must be above 10^4 cm^{-1} , and above 10^5 cm^{-1} is preferred. [26, 30] Materials presented in this thesis will be evaluated according to how sharply the measured absorption coefficient rises to 10^5 cm^{-1} . It is considered good absorption if α reaches 10^5 cm^{-1} within 1 eV of the bandgap. Increasing α allows thinner absorber layers to be used. This decreases the material cost, device weight, and the distance a photocarrier must travel to be extracted at the cell terminal.

One of the most important quantities affecting charge extraction is diffusion length, L_d . [27, 31] This is the average distance a minority carrier diffuses before being annihilated by recombination with a majority carrier. Thus, photocarriers generated within a diffusion length of the appropriate contact will, on average, be successfully extracted.

From this consideration it is apparent that, in the absence of a drift field, a solar absorber requires a long diffusion length for effective charge extraction. The minority carrier diffusion length for a p-type material is given by, [18]

$$L_d = \left(\frac{k_B T}{q} \mu_n \tau_n \right)^{\frac{1}{2}}, \quad (2.20)$$

where μ_n and τ_n are the minority carrier electron mobility and lifetime, respectively. Therefore, to maximize diffusion length an absorber must exhibit high mobility and long minority carrier lifetime. [30]

In addition to the optical and electronic parameters previously mentioned, restrictions are placed on the specific elements which comprise the absorber material. Specifically, these elements must be affordable, naturally abundant, and non-toxic in order for the material to be marketable. [26] There exists room for improvement over the current leading thin-film solar cell materials (CIGS and CdTe), which contain the costly and/or rare In, Ga, and Te. [27, 32, 33] Use of the toxic heavy metal Cd has also been resisted by some countries because of health safety concerns. Research presented in the ensuing chapters involves alternative materials which do not contain these problematic elements.

3. EXPERIMENTAL TOOLS AND TECHNIQUES

This chapter discusses the theory of all experimental tools and techniques used for this research. It begins with a review of the methods used for growth and modification of films fabricated. A section on thin-film characterization follows, with an overview of all analytical techniques used to determine the film composition and material properties.

3.1 Thin film deposition and processing

This section describes the tools and techniques used for the synthesis of thin films, including pulsed laser deposition (PLD), electron-beam (e-beam) evaporation, and post-deposition annealing. Films examined in this thesis were deposited using PLD or e-beam evaporation and later underwent post-deposition annealing to modify the film stoichiometry and/or crystallinity.

3.1.1 Pulsed laser deposition of thin films

Pulsed laser deposition (PLD) is perhaps the simplest method of growing thin films. [34] Figure 3.1 shows a typical PLD system schematic, consisting of a vacuum chamber containing substrate- and target-holders, and an exterior high-powered pulsed laser used to irradiate the target surface. Laser pulses generate plumes of the source material which deposit onto the surface of a nearby substrate. Particles in this plume have a relatively high kinetic energy compared to evaporative methods of physical vapor deposition (on the order of 10–100 eV compared to 1 eV in molecular beam epitaxy, for example). [35, 36] By rotating the target during deposition, the beam may be effectively rastered across the target surface for uniform eroding of the target. [6] Similarly, substrate rotation may be employed to improve uniformity of film thickness. One benefit of PLD is the decoupling

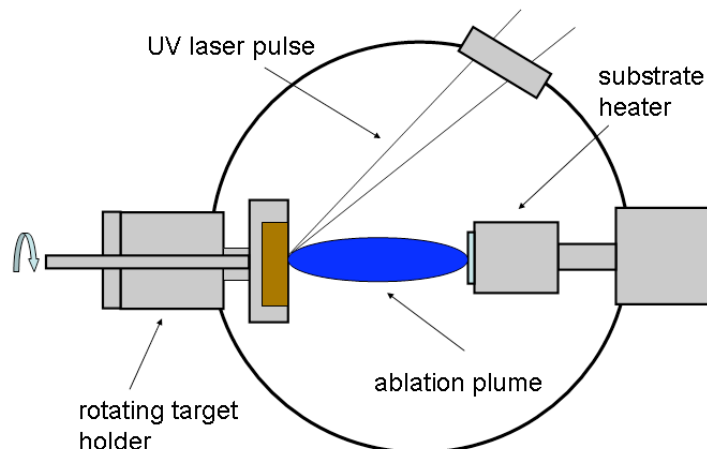


Figure 3.1: Pulsed laser deposition system schematic. [5] Substrate rotation is also present in some systems.

of the energy source, the laser, from the vacuum chamber. This allows one source to be used for multiple deposition chambers.

PLD process parameters are chosen with significant attention given to the reduction of liquid or solid phase particulate in the plume. Vapor phase species are typically in the nanometer range and are desired for smooth films, whereas solid and liquid particulates are in the micron range or larger. [34] Additional goals of PLD processes include achieving high film growth rate, high film uniformity across the substrate, and appropriate film stoichiometry. This is accomplished by adjusting properties of the laser (fluence, wavelength, pulse repetition rate, and number of pulses) and of the deposition environment (substrate temperature, background gas species and partial pressures, and target-substrate distance).

Laser fluence (J/cm^2) on the target can be controlled by modifying the laser power or the spot size. In general, a higher fluence removes more material from the target per pulse, thereby increasing the film growth rate. But care must be taken to avoid the problem of "splashing", in which micron-sized particulate is deposited on the substrate.

[34, 37] Splashing occurs at excessive fluence—both particulate density and average size increase with fluence—and is more prevalent in materials with low thermal conductivity. If splashing can be avoided, high fluence improves film quality at low substrate temperatures by providing kinetic energy to the deposited particles and thereby increasing surface diffusion. Sufficient fluence is also necessary to prevent incongruent evaporation, where the plume is dominated by target elements with lower heats of vaporization (this does not apply to targets comprised of one pure element). In cases where a decrease in fluence is desired it may be advantageous to increase the laser spot size, rather than decrease the laser power, in order to maintain an adequate film deposition rate. Typical fluences of PLD lasers are in the $>1 \text{ J/cm}^2$ range with pulses of 15-45 ns duration. [38]

Laser frequencies used for PLD are typically within the 200–400 nm range, in which most target materials exhibit strong absorption. Longer wavelengths usually penetrate deeper into the target and may contribute to increased splashing. Alternatively, very short wavelengths (and therefore shallow penetration depths) provide incongruent evaporation of the target and low deposition rates. [34]

The repetition frequency of laser pulses (1–100 Hz) is optimized for film smoothness by controlling the rate at which target material arrives at the substrate surface. [34] Studies of superconducting $\text{YBa}_2\text{Cu}_3\text{O}_{7-\delta}$ (YBCO) thin films grown by PLD demonstrated that low repetition rates produced pinholes in films while high rates produced island-like surface outgrowths. Since the total number of laser pulses fired in a deposition is selected to achieve the desired film thickness, it can be seen how increasing the number of pulses per second proportionately increases the deposition rate.

It is clear from the preceding discussion of laser parameters that the ultraviolet wavelengths, high power output, and high pulse rates of excimer lasers render them well-suited for PLD. The electronic transition in excimer lasers is between molecular energy states rather than atomic states as in conventional lasers. Hence, shorter wavelengths and

high efficiencies are achieved. [39] The KrF excimer laser (248 nm) is the most widely used choice for PLD including the research presented in this thesis.

Of the deposition parameters, substrate temperature is one of the most important. [40] Substrate temperature is used in PLD to improve film stoichiometry, crystallinity, and electrical performance. Heating directly increases the surface diffusion coefficient, which allows atoms to find an appropriate lattice site at which to nucleate. [34] This helps preserve the target stoichiometry in the resulting film, since volatile atoms are crystallized immediately and do not re-evaporate when heated by subsequent pulses (as is the case for unbounded atoms). The temperature required to produce monocrystalline films and preserve target stoichiometry is called the critical substrate temperature, T_c . Additionally, studies of lead chalcogenide depositions showed that increasing substrate temperature produced lower carrier concentrations and higher mobilities. Amorphous films are achieved by lowering substrate temperature, which also typically improves film smoothness.

Another method used to affect film stoichiometry is the introduction of a reactive atmosphere during the deposition. Oxygen and nitrogen precursors are employed in cases where films grown under vacuum are deficient of one of those elements. Partial pressures may be as high as 1 torr—the highest of all physical vapor deposition methods. [34] High background pressures can also have detrimental effects on the plasma plume, which is slowed and confined by the reduction in mean free path. This increase in collisions en route to the substrate results in bonding between vapor phase species to form larger particulates. This phenomenon is related to the target-substrate distance, since a longer path traveled by the plume yields more collisions and therefore increased particulate size.

At this point, it is appropriate to mention the specific case of pure metal deposition since it was performed in this research. The multitude of other techniques successfully used to grow metal thin-films (such as sputtering, thermal and e-beam evaporation) leaves

PLD as a less-frequently implemented method. [34] The process differs from the ablation of nonmetals as the laser pulse serves merely to heat the metal to the point of thermal evaporation. This ablation threshold can be particularly large as in the case of refractory metals such as Mo, Re, or W (10 J/cm^2 is reported for W). PLD of metals in general exhibits much lower deposition rates than that of nonmetals.

This discussion of PLD shall conclude with a review of the state of the art. The usefulness of PLD is presently hampered by two major setbacks: large area scale-up, and particulate size. [34, 40] The narrow angular distribution of the plasma plume necessitates the use of very small substrates ($\sim 10 \text{ mm} \times 10 \text{ mm}$). Current approaches to large area scale-up have been explored. One method implements a rotating substrate and target, as well as a programmable mirror which rasters the laser beam across the surface of the target. This effectively moves the plume radially across the substrate to achieve larger coverage, and 125 mm substrates have reportedly been used successfully. The issue of particulate reduction has been addressed by some mechanical systems installed in the vacuum chamber. The general idea is to catch larger plasma species before they reach the substrate. This is made possible by the reduced velocity of such particles, which fall behind their smaller and more desired counterparts. It is apparent that solutions to both problems mentioned here contribute significant complexity to the PLD system. Despite the absence of PLD in commercial production, it has proven to be practical and useful for applications such as the research presented in this thesis.

3.1.2 Electron-beam evaporation

Electron-beam (e-beam) evaporation was used as an alternative to PLD for depositing the thin films discussed in this thesis. The experimental setup, shown in Fig. 3.2, consists of an electron emitting filament, target material, and substrate in a high-vacuum ($\sim 10^{-6}$ Torr) chamber. Electrons are thermionically emitted from the hot filament and

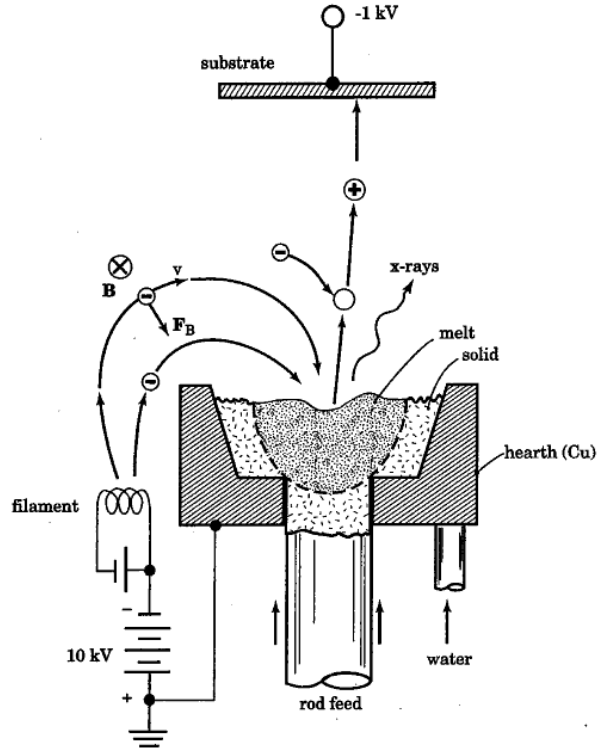


Figure 3.2: Diagram of an electron-beam evaporator. [6]

accelerated through a voltage drop (5–30 kV). [6, 41] The beam is then deflected towards the target by a magnetic field controlled by a solenoid electromagnet. An electron's kinetic energy is transformed to thermal energy upon striking the target, raising the temperature of the material. Evaporation is achieved by sufficiently high electron-beam currents. Vapor phase species are emitted from the target towards a nearby substrate where film growth occurs.

Rather than aiming the beam directly at the target, typical electron-beams are bent through 270° of curvature. [41] This prevents evaporant from depositing on the filament. Electrons are accelerated by the Lorentz force, given by [6]

$$\vec{F} = \vec{F}_E + \vec{F}_B = q_e \vec{E} + q_e \vec{v} \times \vec{B}. \quad (3.1)$$

The force \vec{F}_B is perpendicular to the electron velocity \vec{v} and the magnetic field \vec{B} , as shown in Fig. 3.2. The direction is determined by the right hand rule for vector cross products. Since electronic charge, q_e , is a negative quantity, the resulting \vec{F}_B is in the direction shown. The cyclotron radius of an electron in the beam is inversely proportional to the magnitude of the magnetic field and is given by,

$$r_c = \frac{m_e v_{\perp}}{q_e |\vec{B}|}, \quad (3.2)$$

where m_e is the mass of the electron, and v_{\perp} is the component of \vec{v} perpendicular to \vec{B} . The cyclotron radius may then be modulated to scan the electron-beam across the surface of the target by varying the magnetic field strength. A second solenoid perpendicular to the primary coil is typically used to deflect the electron-beam along a second axis. The beam spot may then be rastered in two dimensions to evaporate a larger area of the target. [38, 42] This utilizes more of the target material and prevents the formation of pits on the target surface, which detrimentally narrow the plume of evaporated material. [6] Maintaining a wide plume is desired for thickness uniformity of resulting thin-films.

The target is contained in a Cu hearth, which is water-cooled to prevent melting. Some systems feed solid rods of target material through the bottom of the hearth as shown in Fig. 3.2. This increases the volume of material available for use before refilling. [6] As an alternative to rod-feeding, target materials may be housed in crucible liners constructed of graphite or other materials. [6, 42] Such liners provide additional thermal insulation between the target and the hearth to increase evaporation efficiency. Targets may then be removed from the deposition chamber. Unlike resistance-heated thermal evaporation, e-beam evaporation only vaporizes a small localized area of the target. This prevents alloying between the target and container materials, thereby reducing contamination. [38]

Substrates may be heated and negatively biased to affect resulting films. Similar to PLD, substrate heating may be used to improve film stoichiometry and crystallinity. Substrate heating increases grain size and prevents the formation of columnar morphology

which is sometimes observed on the surfaces of films thicker than $1\text{ }\mu\text{m}$. [43] Studies have also shown that negatively biasing the substrate ($-1\text{--}4\text{ kV}$) during deposition may reduce the formation of columns as well. Substrate rotation is also commonly used to improve film thickness uniformity.

One valuable benefit of e-beam evaporation is its ability to deposit a wide range of target materials. [6, 41, 42] The high energy densities achievable with electron-beams may evaporate any solid material. Incongruent evaporation may occur in multi-compound materials, producing non-stoichiometric films. [42] But this is avoided with sufficiently high beam current (and thus target temperatures) to evaporate all target species. E-beam evaporation also benefits from a relatively large plume of evaporant compared to that of PLD, providing coverage over a larger area. Research presented in this thesis benefited from each e-beam deposition producing four 1 in^2 substrates, whereas PLD produced one 1 cm^2 per deposition and showed poor thickness uniformity across that area compared to e-beam.

For targets fabricated by sintering polycrystalline powder into pellets, densification is important for congruent evaporation of the target. [44] Additionally, voids formed by gas pockets in source pellets may explode upon heating, resulting in *macroparticle spitting*. [6, 44] Macroparticles are solid or liquid species $0.1\text{--}1\text{ }\mu\text{m}$ in diameter which increase surface roughness of deposited films.

3.1.3 Post-deposition annealing

Post-deposition annealing of thin films may be used for two purposes: to enhance the crystallinity of the film or to modify the material stoichiometry. [45] Stoichiometry modification was desired from the annealing performed in this thesis research, as PLD repeatedly failed to provide the desired stoichiometry. As-deposited films were annealed in sealed glass tubes containing a particular ambient atmosphere.

In post-deposition annealing, the as-deposited film is inserted into a glass tube containing some powder of one or more elements. The tube is then sealed under a vacuum of approximately 100 mT and heated to a desired temperature which exceeds the heat of vaporization of the powder at the appropriate pressure. Once vaporization is achieved the atmosphere may react with the film, provided that the temperature also exceeds that necessary to promote such a reaction.

3.2 Thin-film characterization

The synthesis of thin-films using the processes discussed above is followed by material analysis using several techniques. Methods of characterization include crystallographic, electrical, and optical procedures, all of which are described in this section. Samples first underwent x-ray diffraction to verify that the desired stoichiometry is achieved. This is followed by Hall effect measurements to determine several electrical parameters, and lastly optical characterization to address the material's potential as a solar absorber.

3.2.1 X-ray diffraction

X-ray diffraction (XRD) is a physical technique used to determine the physical structure and composition of powders and single crystals. [7, 35] Bond lengths, bond angles, and the relative position of atoms and ions in the unit cell are determined by this method. X-rays are used since their wavelength is comparable to the interatomic distances in crystals (~ 100 pm). Figure 3.3 shows the diffraction of x-rays from parallel crystal planes separated by distance d . X-rays are elastically scattered by electrons in the structure, and a difference in path length results. Bragg's equation provides the condition for constructive interference,

$$2d \sin(\theta) = n\lambda, \quad (3.3)$$

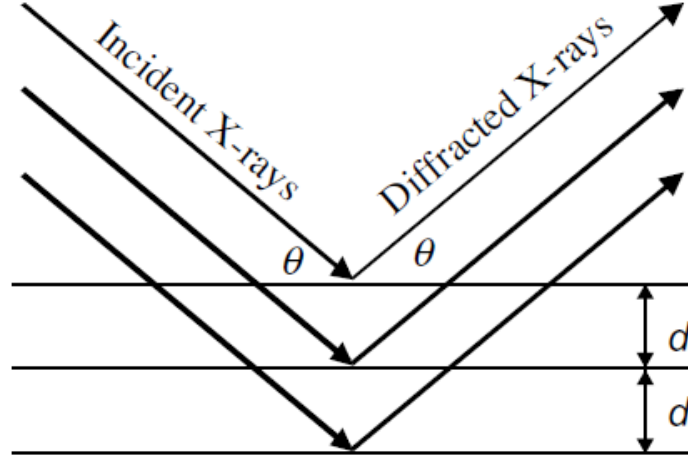


Figure 3.3: Diffraction of x-rays by a crystalline structure. [7]

where θ is the angle of incidence with respect to the crystal plane, λ is the wavelength of incident x-rays, and n is an integer. By sweeping the angle θ over a range ($\sim 5\text{--}30^\circ$) and measuring the reflected intensity, a diffraction pattern is obtained which is specific to the compound being analyzed. Figure 3.4 depicts the nature of diffraction patterns obtained by this method. It is evident that the crystallinity of a sample can be evaluated, since the sharp peaks in intensity shown for crystals are absent in the pattern for the amorphous material. By using a database of patterns obtained from known materials for comparison, stoichiometry can quickly be identified using XRD.

3.2.2 Hall effect measurement

Hall effect measurements are used to determine the majority carrier type, concentration, and mobility in a material. [24, 38, 46, 47] The premise of the Hall effect is the Lorentz force, which is exerted on any charged particle moving through a magnetic field.

Figure 3.5 shows the experimental configuration for an n-type sample of physical dimensions $d \times l \times w$. The current I_x is achieved by the applied potential V_x and hence

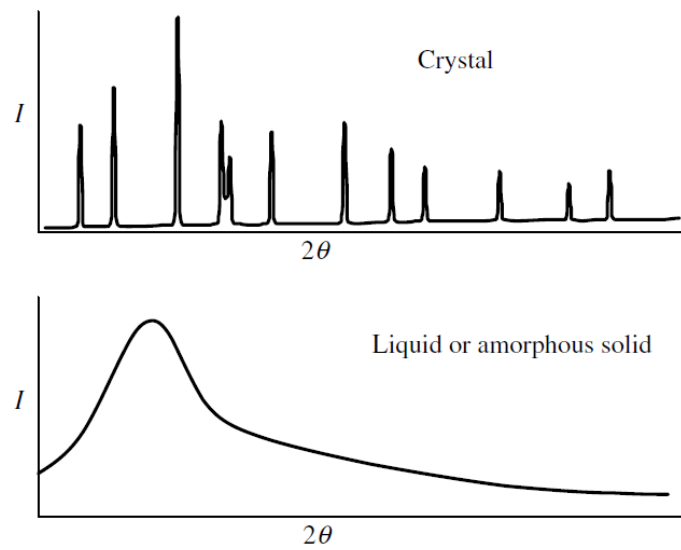


Figure 3.4: Example XRD diffraction patterns for crystalline and amorphous solids. Intensity is plotted vs. 2θ by convention. [7]

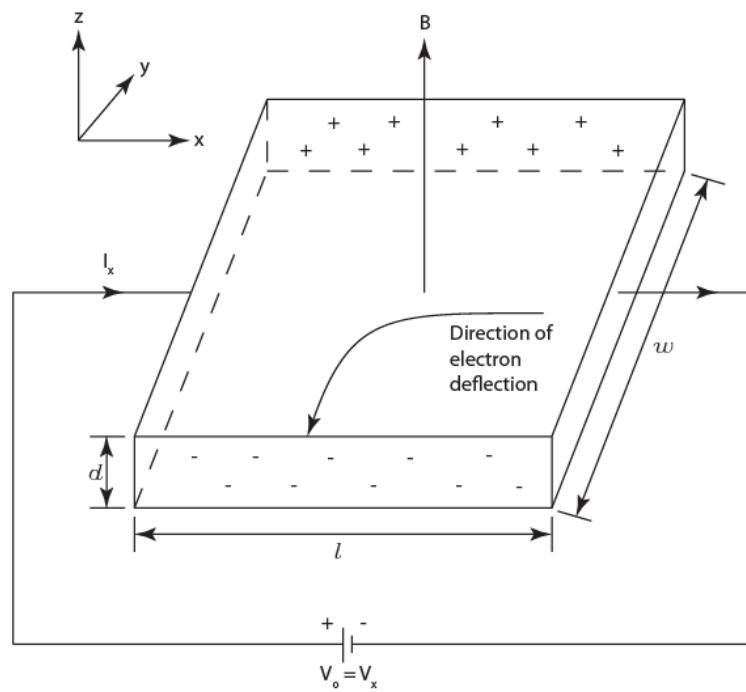


Figure 3.5: Experimental configuration for the Hall effect measurement. [8]

an electric field E_x . The magnetic field \vec{B} is directed along the z-axis. A force \vec{F} is thus exerted on the electrons in the material according to the Lorentz force [8, 45, 47],

$$\vec{F} = q(\vec{E} + \vec{v}_n \times \vec{B}), \quad (3.4)$$

where q is the charge of the particle (in this case an electron of charge $-q$), \vec{E} is the applied electric field in the x-direction, and \vec{v}_n is the electron drift velocity. Note that the direction of electron flow is opposite that of conventional current. The Lorentz force deflects the path of electrons towards the negative y-direction as they traverse the semiconductor. This deflection induces a Hall voltage V_H along the y-axis, which is assessed in the Hall effect measurement. In a p-type material, majority carrier holes with charge $+q$ would deflect in the same direction as the electrons of the n-type sample. The resulting V_H would accordingly have opposite polarity. The *Hall coefficient* is given by

$$R_H = -\frac{V_H d}{I_x B}, \quad (3.5)$$

with the sign of R_H indicating the type of majority carrier ($R_H > 0$ for p-type and $R_H < 0$ for n-type). Its magnitude is used to calculate carrier concentration by the relation

$$\begin{aligned} R_H &= \frac{1}{qn_o} && \text{for electrons, and} \\ &= \frac{1}{qp_o} && \text{for holes,} \end{aligned} \quad (3.6)$$

where n_o and p_o are the equilibrium electron and hole concentrations, respectively. Hall mobility is then given by

$$\mu_H = \frac{l}{w} \left(\frac{V_H}{V_x B_z} \right). \quad (3.7)$$

In practice, the Hall mobility is higher than the conduction mobility due to errors arising from contacts of a finite size and location within the periphery of the sample. [8] These effects may be reduced by employing shadow masks with a cross pattern to deposit thin films, or by increasing B_z or V_x . [5, 45, 47]

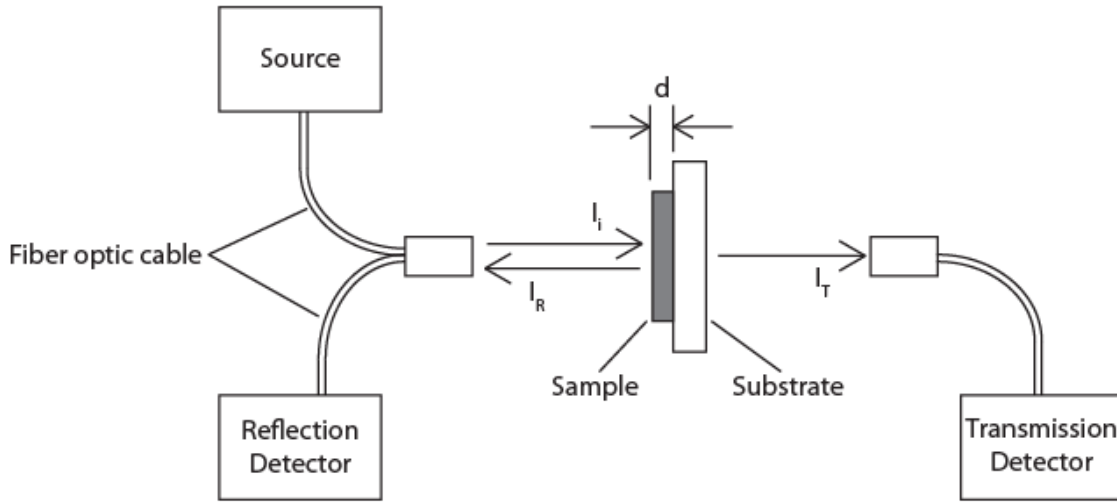


Figure 3.6: Experimental setup for measuring transmitted and reflected intensities.

3.2.3 Optical transmission and reflection

Optical tests were performed on thin-films to determine the material's optical band gap, E_G , and absorption coefficient, α . Substrates used for this technique must be transparent to the wavelengths of interest, such as fused silica.

Figure 3.6 shows the experimental setup for the measurement. The source provides incident light of intensity I_i and wavelength λ , which propagates through a fiber optic cable and is emitted normal to the sample of thickness d . The light reflected back towards the left is coupled into another optical fiber and propagates to the reflection detector where its intensity, I_R , is measured. For samples with high surface roughness, diffuse reflection will serve to lower the detectable reflection intensity. In order to achieve high accuracy, reflection should be as specular as possible. [48] Intensity of the transmitted light, I_T is measured by the transmission detector in a similar fashion. Transmittance (T) and reflectance (R) are percentages of these measured intensities compared to the incident

beam, and are functions of wavelength:

$$\begin{aligned} T &= \frac{I_T}{I_i} \\ R &= \frac{I_R}{I_i}. \end{aligned} \quad (3.8)$$

The absorption coefficient may then be approximated according to Beer's Law, [48]

$$\frac{T}{1-R} = e^{-\alpha d}. \quad (3.9)$$

The measurement is executed over a range of wavelengths and the material's band gap is determined by plotting absorption coefficient vs. incident photon energy. [23] For indirect band gap materials, $\alpha^{\frac{1}{2}}$ is plotted vs. $h\nu$. The band gap is determined by extrapolating the curve to intercept the x-axis. A similar method is used for direct band gap materials by plotting α^2 vs. $h\nu$.

The system used for research presented in this thesis employed an InGaAs detector for the near-infrared (NIR) range (800–2600 nm) and a Si detector for the ultraviolet/visible (UV/V) range (200–1100 nm) for a total combined range of 200–2600 nm. [48] The UV/V source used both deuterium (250–450 nm) and halogen (450–1000 nm) lamps. The NIR source was a halogen lamp (1000–2200 nm).

3.2.4 X-ray reflectivity (XRR)

X-ray reflectivity (XRR) measurements were used to determine thickness, density, and surface roughness of both single layer and multilayer thin-films. [49, 50] In XRR, incident x-rays are emitted towards the sample and impinge on the surface at angle ω with respect to the plane, as shown in Fig. 3.7. While some rays are reflected at the film surface, others propagate through the material and reflect at the film-substrate interface. [51] Interference occurs between the two rays, and can be observed by plotting reflectivity vs. ω or 2Θ as shown in Fig. 3.8. A computer-based model is generated to fit the experimental data and determine the properties of the sample. Film density is extracted

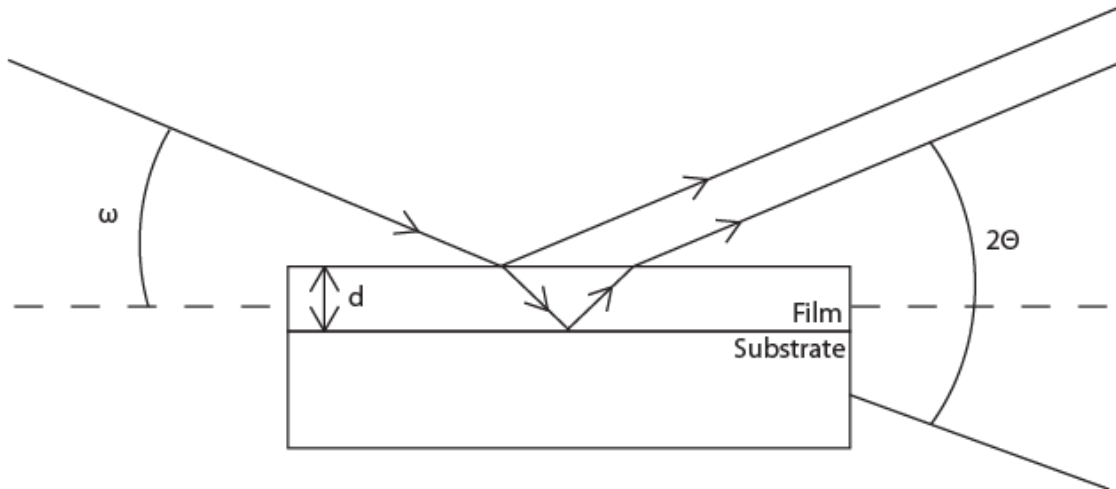


Figure 3.7: X-ray reflection at the thin-film surface and film-substrate interface.

from the critical angle, at which a sharp drop in reflectivity occurs. The distance between reflectivity maxima indicates film thickness. Average slope in the decay of reflectivity is related to surface roughness, and the difference in density between layers and interface roughness can be determined from the oscillation amplitude. [9]

3.2.5 Spectroscopic ellipsometry (SE)

Spectroscopic ellipsometry (SE) is an optical characterization technique which may be used even for samples on metallic or other non-transparent substrates. Light reflected from the sample is measured to determine the material thickness, complex index of refraction, dielectric constant, absorption coefficient, and band gap. [52] A multitude of material types can be characterized with SE, including dielectrics, semiconductors, metals, and multilayered structures. [53] SE differs from other types of ellipsometry in its capacity to use a range of wavelengths and generate spectra from measured data. [23] Measurements in the ultraviolet, visible, and infrared ranges are all commonly used.

The setup, shown in Fig. 3.9, uses a monochromator to generate incident light of wavelength λ . This light propagates through a fiber optic cable to the input unit, where it

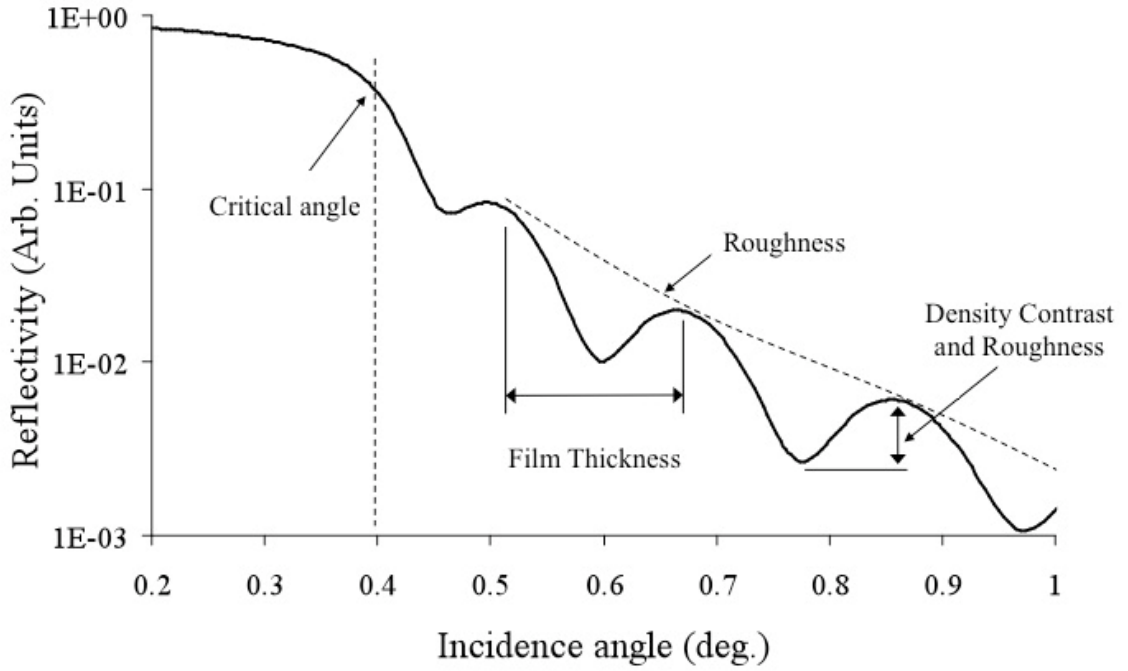


Figure 3.8: Plot of x-ray reflectivity vs. incidence angle. [9]

is emitted towards the sample. Reflected light is received by the detector unit as shown in Fig. 3.10. The goniometer base controls the rotation of the source and detector units relative to the sample stage in order to achieve a range of incidence angles.

Incident light impinging on the sample is linearly polarized with equal amplitudes of both s- and p-polarizations. [52, 54] After reflection by the sample, the detected light has s- and p- polarizations which may be out of phase and of different amplitudes. Parameters of interest are the amplitude ratio, Ψ , and the phase difference, Δ . [52, 55] Ψ and Δ are related by the equation,

$$\tan(\Psi) \exp(i\Delta) = \left(\frac{N_1 \cos \Theta_0 - N_0 \cos \Theta_1}{N_1 \cos \Theta_0 + N_0 \cos \Theta_1} \right) / \left(\frac{N_0 \cos \Theta_0 - N_1 \cos \Theta_1}{N_0 \cos \Theta_0 + N_1 \cos \Theta_1} \right), \quad (3.10)$$

where N_0 and N_1 are the complex refractive indices of air and the sample, respectively, and Θ_0 and Θ_1 are the angles of incidence on the film surface and film-substrate interface, respectively. This relationship is used to determine the complex refractive index of the

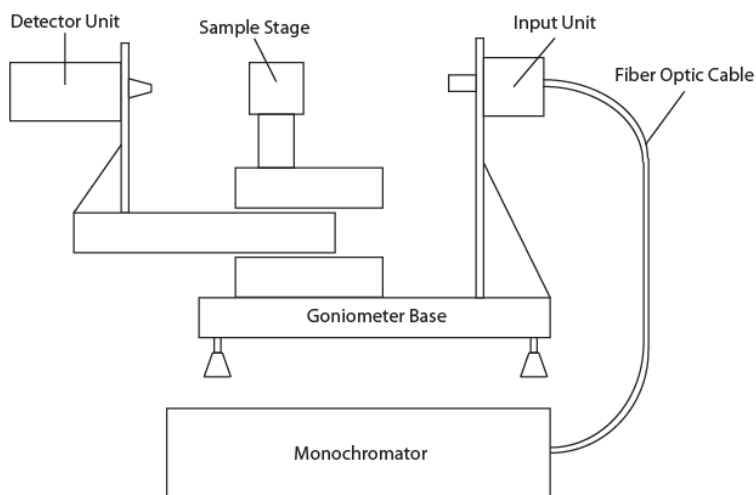


Figure 3.9: Variable angle spectroscopic ellipsometer tool schematic. An external control box (not shown) controls the detector unit and sample stage rotation.

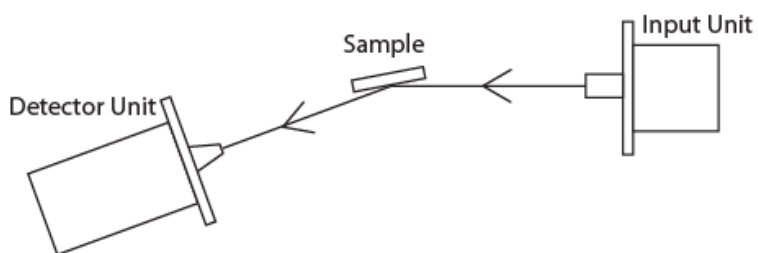


Figure 3.10: Overhead view of the variable angle spectroscopic ellipsometer, showing the reflection of light incident on the sample.

film. The imaginary part of the refractive index, the extinction coefficient k , is used to determine the absorption coefficient, α .

$$\alpha = \frac{4\pi k}{\lambda} \quad (3.11)$$

By plotting α vs. incident photon energy, the onset of absorption and thus the band gap of the material is determined. [53]

3.2.6 Photoelectrochemical (PEC) cell measurements

As an alternative to fabricating an entire solar cell, performance of the absorber may be evaluated through the synthesis of a photoelectrochemical (PEC) solar cell. A PEC cell uses a liquid electrolyte to form a rectifying junction with the absorbing semiconductor, [56, 57] as shown in Fig. 3.11.

A PEC cell is made by connecting the semiconducting photoelectrode to a metal counter electrode via an external circuit. Both of these electrodes are then submerged in an electrolyte containing a redox couple, forming the device depicted in Fig. 3.11. [57] Similar to the Schottky barrier, band-bending occurs to bring the device into a state of equilibrium with the photoelectrode's Fermi level aligning with the electrolyte's redox potential, E_{redox} . [56] Light of energy $h\nu$ incident on the photoelectrode generates photocarriers, with the minority carrier holes traveling to the electrolyte where an oxidation reaction occurs ($A^- \rightarrow A$). Similarly, the photogenerated majority carrier electrons travel through the external circuit to the counter electrode, where the opposite reaction occurs ($A \rightarrow A^-$).

Several important parameters regarding solar cell performance may be extracted from PEC cell current-voltage measurements, including short-circuit current (I_{SC}), open-circuit voltage (V_{OC}), fill factor (FF), and the cell conversion efficiency. [57]

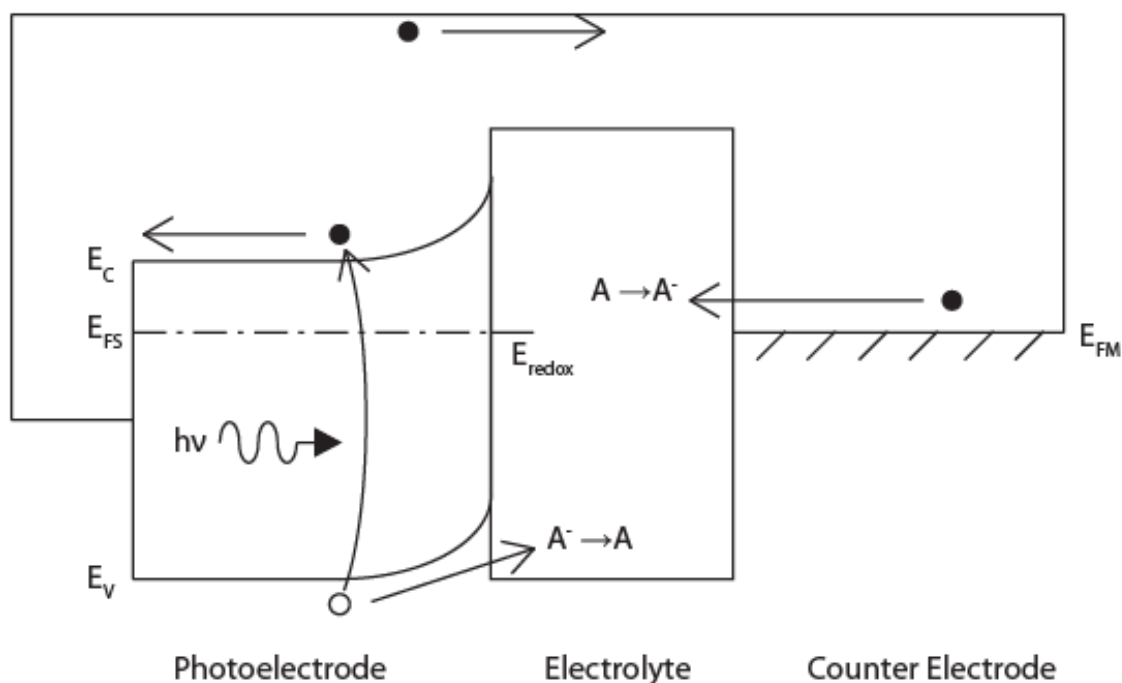


Figure 3.11: Energy band diagram of a PEC cell with an n-type photoelectrode and electrolyte containing the redox couple A, A^- .

3.3 Conclusion

This chapter provides an overview of experimental methods used for synthesis and characterization of materials presented in this thesis. Techniques used for deposition of thin-films are first discussed, including pulsed laser deposition and electron-beam evaporation. A description of post-processing techniques for modification of precursor stoichiometry follows.

The various analytical techniques discussed in this chapter consist of optical and electrical analysis. Many of the important material parameters for solar absorbers (as discussed in Chapter 2) are determined using these techniques. Material bandgap, absorption coefficient, carrier type and concentration, and mobility may all be determined through the combined use of optical transmission and reflection, variable angle spectroscopic ellipsometry, and Hall effect measurements. Additional information about material

identification and absorber performance may be determined using x-ray diffraction, x-ray reflectivity, and PEC measurements.

4. Cu₃PSe₄ THIN-FILMS

Cu₃PSe₄ has been a material of interest for potential solar absorber application for over 20 years, and its crystal structure was first reported almost 20 years before. [30, 58] In addition to a favorable bandgap and high optical absorption, Cu₃PSe₄ lacks both indium and tellurium, which are rare and expensive. The cost of large-scale production of Cu₃PSe₄ devices could therefore be lower than that of the popular CdTe and Cu(In,Ga)Se₂ (CIGS) solar cells.

This chapter begins with a summary of previously known material properties of Cu₃PSe₄ supporting its candidacy as a solar absorber. Data acquired from polycrystalline powder samples at Oregon State University is included. A discussion of thin-film fabrication follows, including preliminary failures and eventual successes in synthesizing Cu₃PSe₄ thin-films. Finally, electrical and optical characterization of synthesized thin-films is presented.

4.1 Introduction

Interest in Cu₃PSe₄ as a potential solar absorber was documented as early as 1991, when single-crystal measurements demonstrated a direct bandgap of 1.4 eV, p-type conduction with carrier concentrations of $10^{16} - 10^{17} \text{ cm}^{-3}$, mobilities of $20 \text{ cm}^2/\text{Vs}$, and an absorption coefficient above 10^5 cm^{-1} . [30] The Cu₃PSe₄ crystal structure is the wurtzite-based enargite (Cu₃AsS₄) structure, with an orthorhombic unit cell as shown in Fig. 4.1. [10, 30, 58, 59, 60] Its lattice parameters are $a = 7.685 \text{ \AA}$, $b = 6.656 \text{ \AA}$, and $c = 6.377 \text{ \AA}$.

Figure 4.2 shows the calculated energy band structure for Cu₃PSe₄, with a direct bandgap of 1.38 eV at the Γ point. [10] This value is in close agreement with diffuse reflectance measurements of polycrystalline powder samples, which indicated an optical

bandgap of 1.4 eV. Both of these values are well within the range of desired bandgaps for solar absorbers (1.3–1.6 eV). [30]

Optical absorption of Cu_3PSe_4 is comparable to that of GaAs and CIGS. [10] The calculated absorption coefficient, α , for Cu_3PSe_4 is shown in Fig. 4.3 along with measured data for GaAs and CIGS for comparison. Absorption for Cu_3PSe_4 exceeds 10^5 cm^{-1} for incident photon energies above 2.6 eV, and is greater than that of GaAs over the range $520 < \lambda < 660 \text{ nm}$. Although the absorption coefficient of CIGS is greater than that of Cu_3PSe_4 , its bandgap is significantly lower (1.15 eV). This detrimentally limits the attainable open-circuit voltage for CIGS solar cells, as discussed in Chapter 2.

The calculated absorption coefficient is used to determine the *spectroscopically limited maximum efficiency (SLME)* of Cu_3PSe_4 , shown in Fig. 4.4. SLME is an expansion on the Shockley-Queisser limit for solar cell efficiency, which is dependent only on the material's bandgap. By considering the effects of nonradiative recombination processes, the AM1.5 solar spectrum, and absorption coefficient, SLME provides a method of screening potential absorber materials. [28] Solar cell efficiency for Cu_3PSe_4 is shown as a function of absorber layer thickness. For absorber layers over 500 nm in thickness the maximum efficiency exceeds 28% . Since this value is significantly higher than the currently achieved maximum efficiencies of the leading thin-film solar cell technologies, Cu_3PSe_4 is a viable absorber material.

The previously described electrical and optical data from crystalline and polycrystalline samples forms the premise for interest in Cu_3PSe_4 as a solar absorber. The purpose of the research presented in this chapter is to fabricate Cu_3PSe_4 thin-films and evaluate their performance for use in thin-film solar cells.

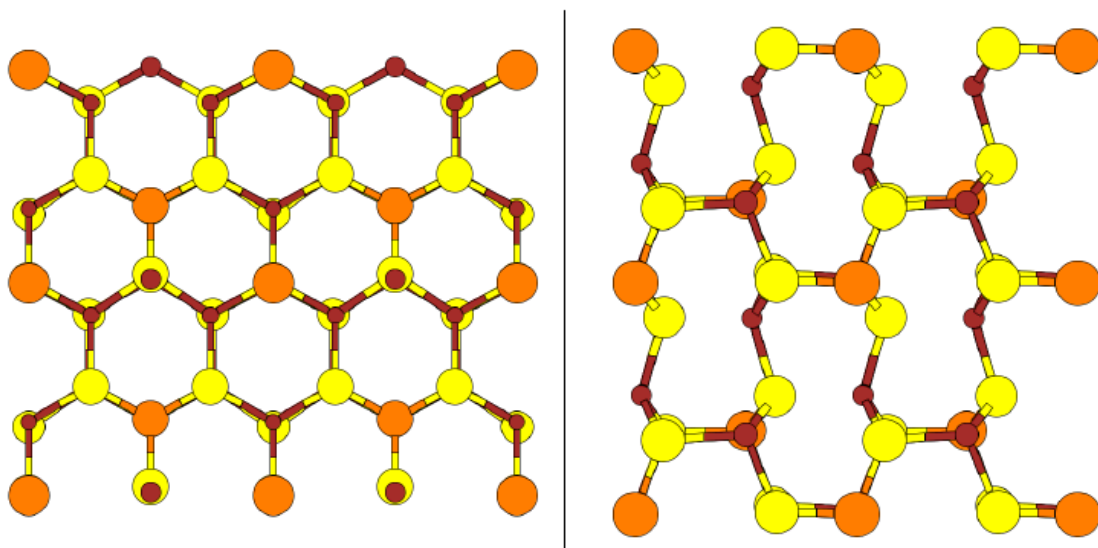


Figure 4.1: Enargite crystal structure for Cu_3PSe_4 , showing Cu (orange), P (red), and Se (yellow) atoms.

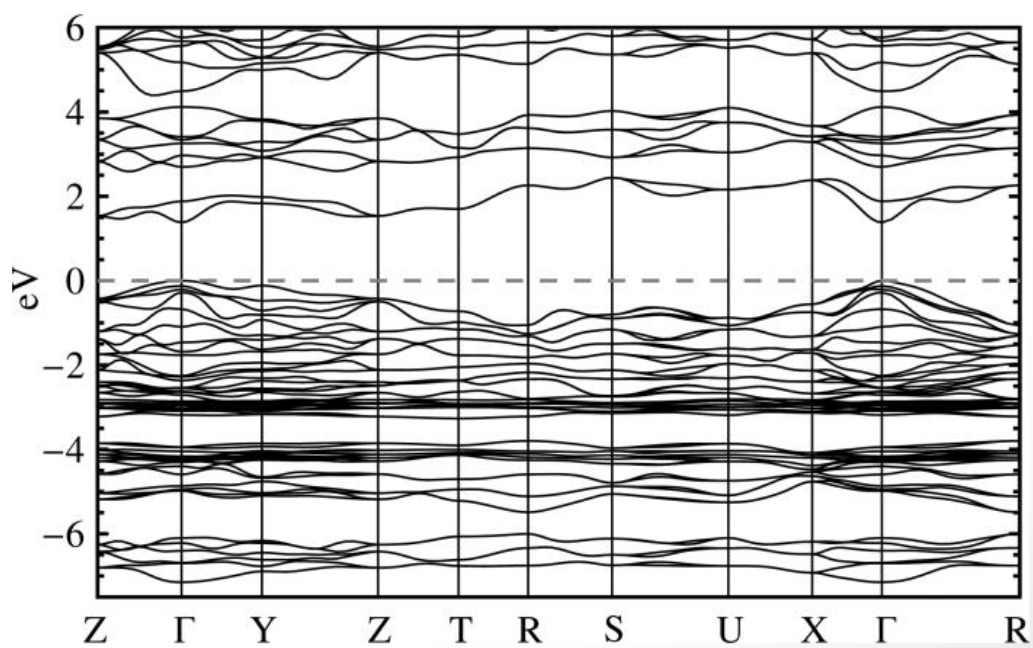


Figure 4.2: Calculated energy band structure for Cu_3PSe_4 . [10]

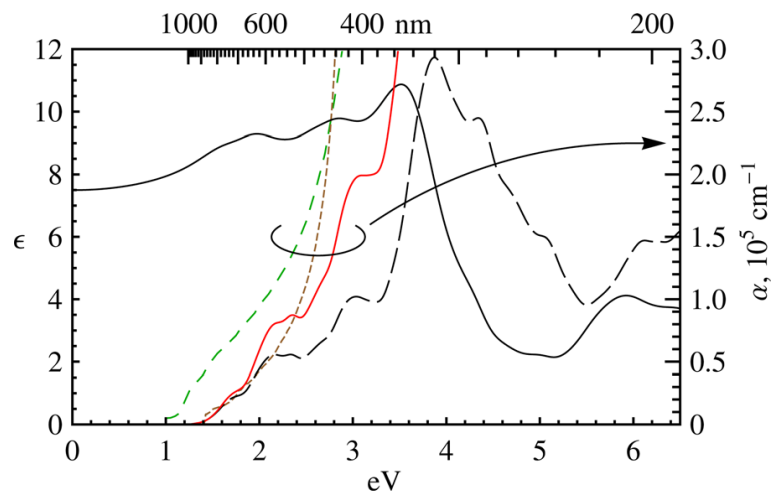


Figure 4.3: Calculated absorption coefficient for Cu_3PSe_4 (red) along with experimental data for GaAs (brown dashed) and CIGS (green dashed). The real (solid) and imaginary (long-dashed) parts of the dielectric function ϵ are also shown. [10]

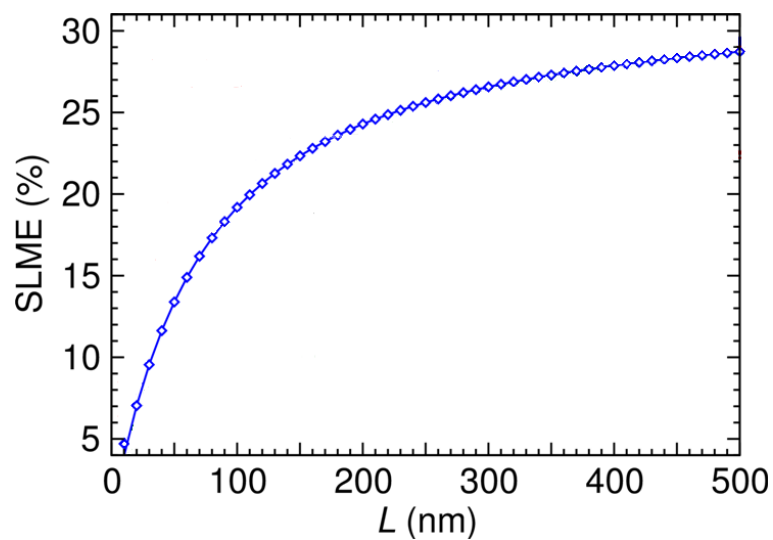


Figure 4.4: Calculated spectroscopically limited maximum efficiency (SLME) versus absorber layer thickness for Cu_3PSe_4 solar cells. [11]

4.2 Experiment

This section delineates the experimental progression towards eventual success in synthesizing Cu_3PSe_4 thin-films. The process included four experimental stages. Initially, pulsed laser deposition (PLD) process parameters were varied in an attempt to deposit phase-pure Cu_3PSe_4 without post-processing. Secondly, post-deposition annealing was used to modify film stoichiometry. A variety of substrates were then employed to improve film smoothness and adhesion. Finally, the anneal procedure was modified to further improve film quality.

4.2.1 Pulsed laser deposition parameters

Pulsed laser deposition (PLD) process parameters were varied to observe their effects on resulting samples. A study of substrate heating was first performed, with depositions spanning the temperature range of 25–500 °C. The effect of varying laser fluence from 1 to 2.3 J/cm² was then observed for constant substrate temperature. All films discussed were deposited by ablation of a polycrystalline Cu_3PSe_4 pressed pellet using a laser repetition rate of 7 Hz. The effects of substrate heating and laser fluence were evaluated by comparison of measured XRD spectra for the produced thin-films.

Figure 4.5 shows the measured XRD patterns for films deposited by PLD with various substrate temperatures. All depositions employed a laser fluence of 1 J/cm². Depositions at room temperature produced amorphous films, while heating the substrate to 300 °C produced polycrystalline films composed of the P- and Se-deficient Cu_7PSe_6 phase. Further increasing the temperature served to promote P- and Se-deficiency by introducing the $\text{Cu}_{1.8}\text{Se}$ *Berzelianite* phase. The intensity of Berzelianite peaks increased with substrate temperature between 350 and 450 °C. No P was retained in films deposited on 500 °C substrates, which were phase-pure $\text{Cu}_{1.8}\text{Se}$. At no temperature was the desired Cu_3PSe_4 phase successfully transferred from the target to the substrate.

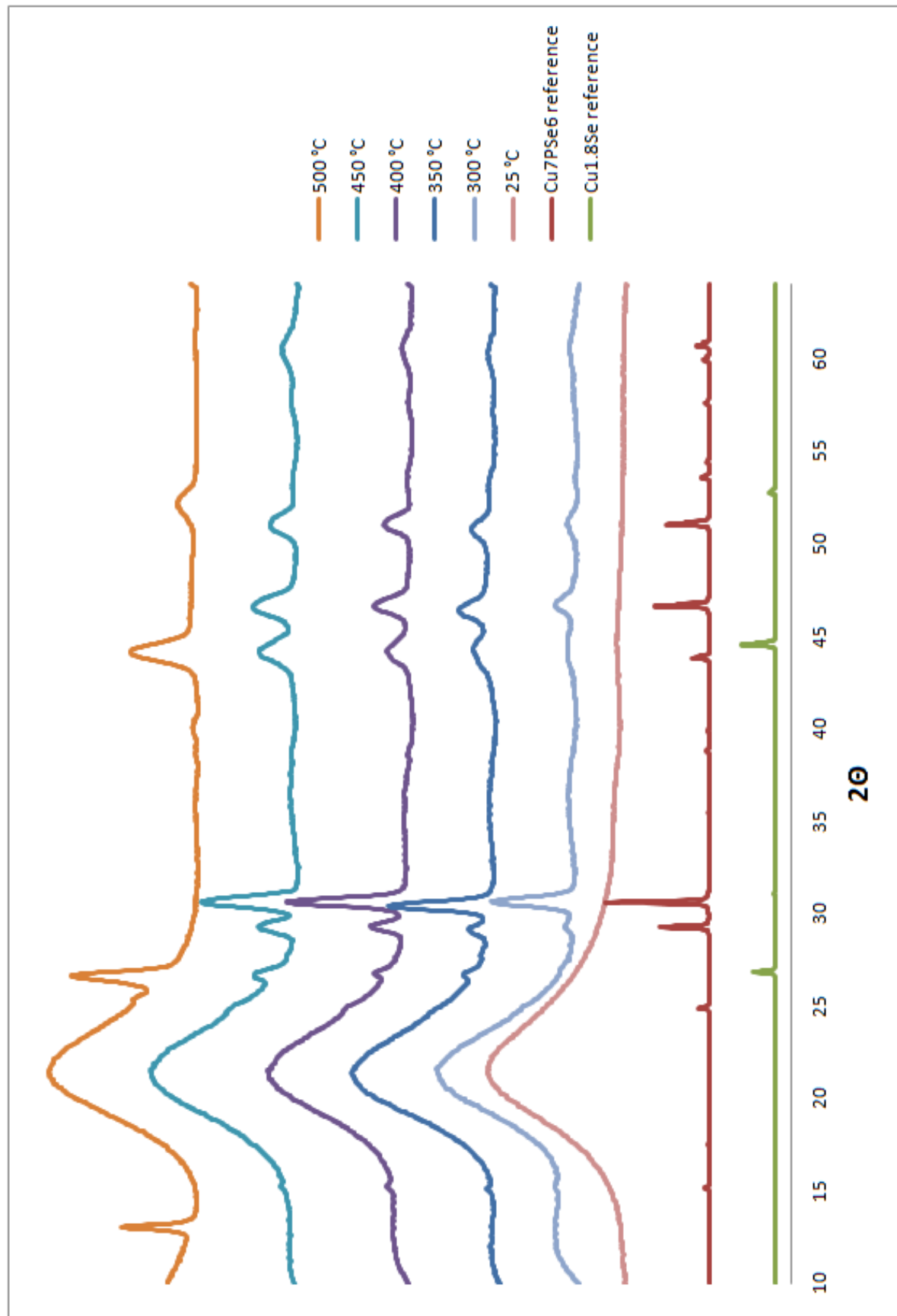


Figure 4.5: Measured XRD spectra for films deposited by PLD at various substrate temperatures. Laser fluence was 1 J/cm^2 . Cu_7PSe_6 (red) and $\text{Cu}_{1.8}\text{Se}$ (green) reference spectra are shown for comparison.

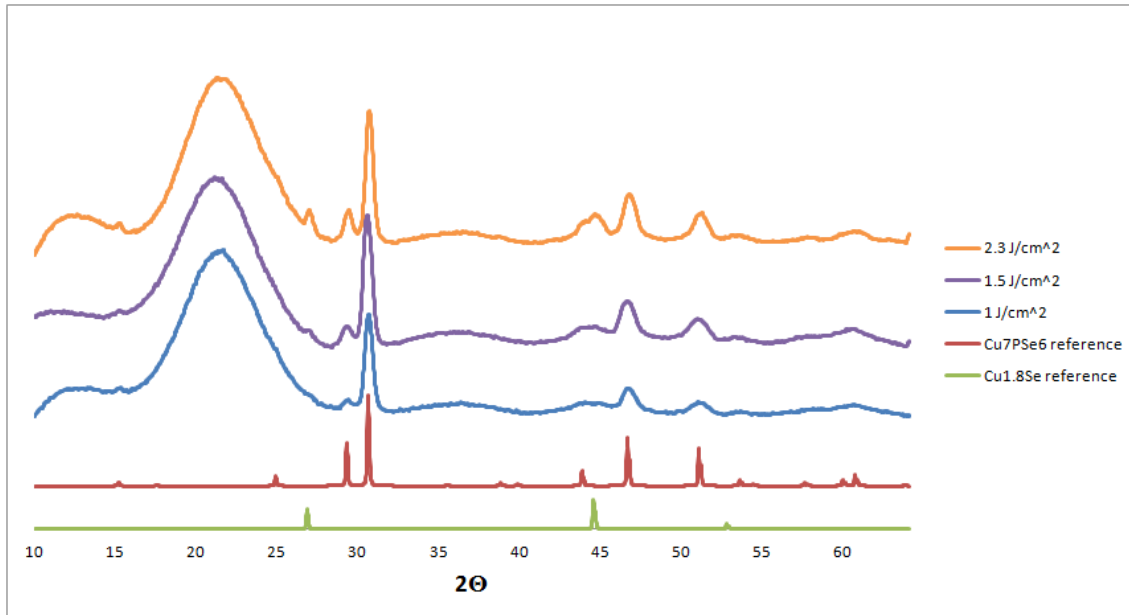


Figure 4.6: Measured XRD spectra for films deposited by PLD at various laser fluences on 300 °C substrates. Cu_7PSe_6 (red) and $\text{Cu}_{1.8}\text{Se}$ (green) reference spectra are shown for comparison.

A study of the effect of laser fluence similarly failed to produce the Cu_3PSe_4 material. Fluence was varied over the range of 1–2.3 J/cm^2 , with substrate temperature held constant at 300 °C. Measured XRD patterns of samples produced are shown in Fig. 4.6. Phase-pure Cu_7PSe_6 samples were deposited using a fluence of 1 J/cm^2 . Increasing the fluence to 1.5 J/cm^2 introduced the $\text{Cu}_{1.8}\text{Se}$ impurity, the concentration of which was increased by further raising the fluence to 2.3 J/cm^2 .

Varying substrate temperature and laser fluence failed to produce Cu_3PSe_4 thin-films as-deposited, with all samples showing P and Se deficiencies. The effects of increasing substrate temperature and laser fluence were similar, both serving to increase the concentration of the $\text{Cu}_{1.8}\text{Se}$ impurity in deposited films. This result is surprising, since substrate heating and high fluence typically improve preservation of the desired stoichiometry and promote stoichiometric vaporization of the target. Subsequent experiments used post-processing anneals to reintroduce P and Se into the films.

4.2.2 Post-deposition anneals in P and Se

Sealed-tube anneals were used to modify the stoichiometry of thin-films deposited by PLD (see Chapter 3). Anneals presented in this thesis were performed on films containing Cu_7PSe_6 and/or $\text{Cu}_{1.78}\text{Se}$ phases, which were faithfully reproduced by PLD using the process parameters discussed above. Initially, two anneal processes were used; anneal 'A' was performed in a sealed tube containing phosphorus powder, and anneal 'B' was performed in a sealed tube containing both phosphorus and selenium powders. Temperature in both anneals was ramped up to 450 °C at a rate of 2 °C/minute. The temperature was held for 2 hours and ramped down at the same rate. Anneal 'B' successfully produced phase-pure Cu_3PSe_4 films, as determined by XRD. The measured spectrum for such a film on glass is shown in Fig. 4.7.

Although the desired material was successfully synthesized by this method of post-deposition annealing, resulting films consistently showed high surface roughness and poor adhesion to the substrate. Since the as-deposited films grown by PLD were smooth and showed good adhesion, it was determined that the annealing procedure promoted a decrease in film quality. Annealing experiments performed with only Se powder indicated that the film quality was dramatically degraded after the vaporization of Se powder but before the P vaporization.

4.2.3 Effect of different substrate materials

Cu_3PSe_4 thin films were synthesized on a variety of substrate materials to improve film smoothness and adhesion. Initial experiments utilized insulating substrates, such as glass and fused silica, to allow resulting samples to be measured with electrical characterization techniques without electrical conduction occurring in the substrate. Since these materials are transparent to visible wavelengths, they additionally allowed optical transmission measurements to be performed. All Cu_3PSe_4 films grown on these substrates

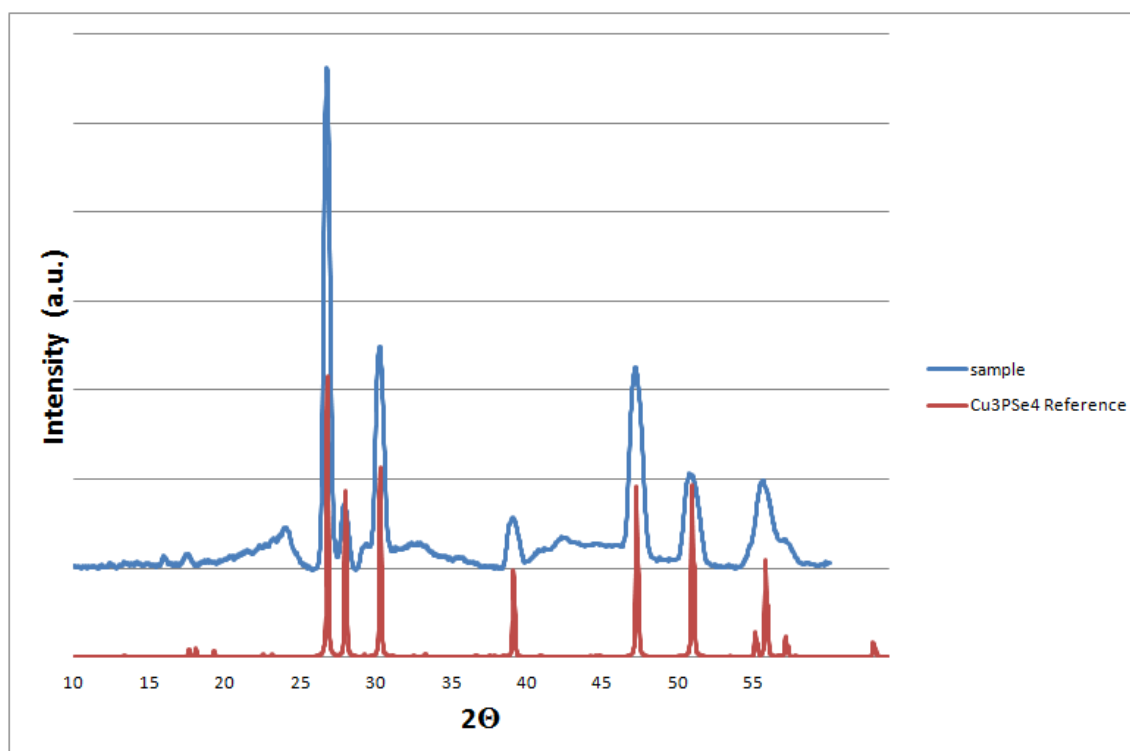


Figure 4.7: Measured XRD spectrum for a Cu_3PSe_4 thin-film sample (blue) and the Cu_3PSe_4 reference spectrum (red) for comparison. The sample was deposited by PLD with a 300 °C substrate temperature and laser fluence of 1 J/cm², and annealed at 450 °C in a P and Se background.

exhibited poor adhesion and smoothness after the annealing procedures discussed above. This is consistent with the documented difficulty in adhering Cu metallization layers to many dielectrics. [38, 61]

The transparency and insulating qualities of dielectric substrates were sacrificed in order to improve adhesion. Several materials are known to be adhesion promoters between Cu and SiO₂, including Cr, Ti, Nb, Al, and Mg. [38, 61] Of these, Ti and Al are the most readily available for deposition by thermal evaporation at Oregon State University. Higher work-function metal substrates are preferred for deposition of p-type semiconductors in order to promote ohmic contact formation, as described in Chapter 2. Therefore, Ti was chosen for its higher work-function than Al ($\phi_{Ti} = 4.33$ eV, $\phi_{Al} = 4.1$ eV). [24, 62] Post-deposition anneals of films deposited by PLD on Ti substrates succeeded in synthesizing Cu₃PSe₄ with improved adhesion and smoothness compared to films on glass. Similar results were achieved on titanium nitride (TiN), commonly used as a diffusion barrier material between Cu and SiO₂. [63, 64, 65]

Although Mo is not a typical adhesion promoter for Cu thin-films, its relatively high work-function (4.6 eV) and tendency to form MoSe₂ make it a popular back contact material for CIGS solar cells. [15, 26] Experiments performed with Mo substrates succeeded in synthesizing Cu₃PSe₄, although the film roughness was greater than that of films deposited on Ti.

Although the use of an alternative substrate material improved the adhesion and smoothness of annealed films, they remained too diffuse for optical characterization techniques to be used. Modification of the anneal procedure was necessary for achieving higher quality Cu₃PSe₄ films.

4.2.4 Post-deposition anneals with P_4Se_3 powder

The anneal procedure was revised in an attempt to improve film smoothness and adhesion. P_4Se_3 powder was acquired and used in subsequent anneals as an alternative to both P and Se powders. Since P_4Se_3 has a reported melting point of 246 °C, the necessary annealing temperature was reduced to 200 °C under vacuum. [66] Dissociation of the P_4Se_3 molecule provided gas phase P and Se atoms simultaneously, thereby avoiding an initial selenization and subsequent phosphorization of the film.

Figure 4.8 shows the measured XRD patterns for thin films resulting from sealed tube anneals with P_4Se_3 powder at various temperatures. Temperatures of 200 °C or greater were required to synthesize phase-pure Cu_3PSe_4 samples. The Cu_7PSe_6 impurity phase was observed in samples annealed at 175 °C, even for hold times increased to 3 hours. Excessively high temperature anneals (450 °C) produced samples with a high degree of crystallinity, observed in the tall, narrow peaks measured by XRD. Such samples were essentially layers of polycrystalline powder coating the substrate. They demonstrated poor material quality, with extremely high surface roughness and poor adhesion.

Anneals at 200 °C produced the highest quality Cu_3PSe_4 thin-films. Samples annealed at this temperature maintained strong adhesion to fused silica substrates and low surface roughness. The use of transparent, insulating substrates allowed optical transmission and electrical characterization of these thin-films.

4.3 Characterization of thin-films

This section includes the optical and electrical characterization Cu_3PSe_4 thin-films synthesized by PLD and post-deposition annealing at 200 °C with P_4Se_3 powder.

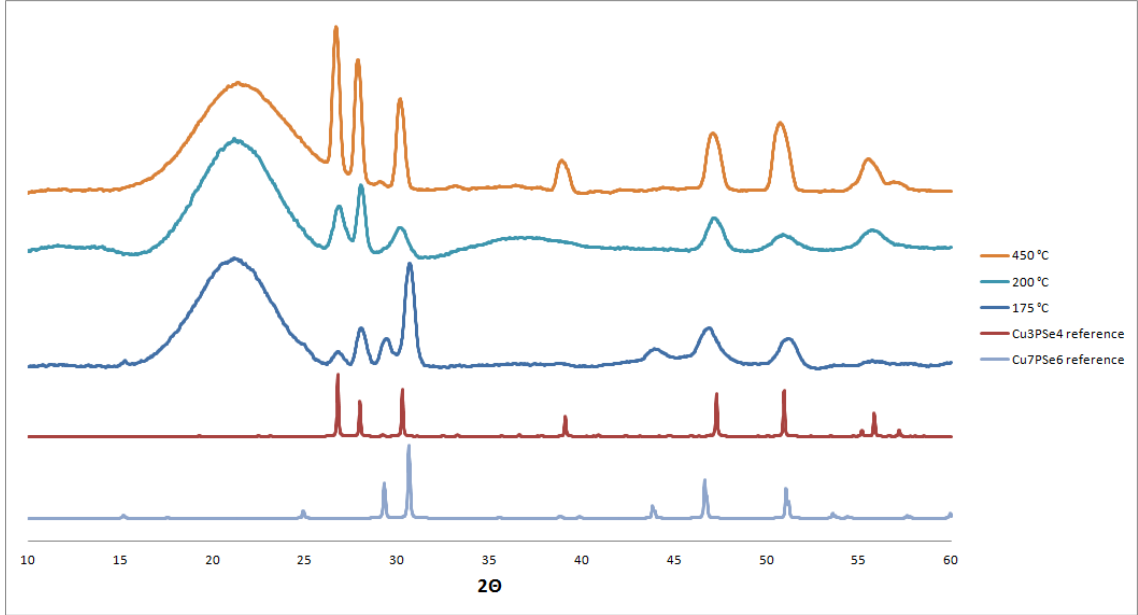


Figure 4.8: Measured XRD spectra for samples annealed at different temperatures.

4.3.1 Optical transmission and reflection

The measured absorption coefficient (α) of Cu_3PSe_4 thin films is shown in Fig. 4.9. The observed optical bandgap is ~ 1.2 eV, indicated by the large increase in α at this energy. Although this bandgap is less than the calculated value of 1.38 eV, it is still within the range of acceptable bandgaps for solar cell absorber materials. The absorption coefficient reaches a satisfactory value of 10^5 cm^{-1} for photon energies $> \sim 2.5$ eV, but the turn-on is more gradual than is desired. Absorption reaches 10^5 cm^{-1} at photon energies ~ 1.3 eV above E_g , where the transition is preferred to occur within 1 eV.

4.3.2 Electrical characterization

Electrical characterization of Cu_3PSe_4 thin-films included Hall effect and four-point probe measurements. Hall effect measurements indicated p-type conduction, with hole concentrations of $3.3\text{--}4.9 \times 10^{16} \text{ cm}^{-3}$. These values are within the range of acceptable carrier levels for solar absorbers ($10^{14}\text{--}10^{16} \text{ cm}^{-3}$). Measured hole Hall mobilities

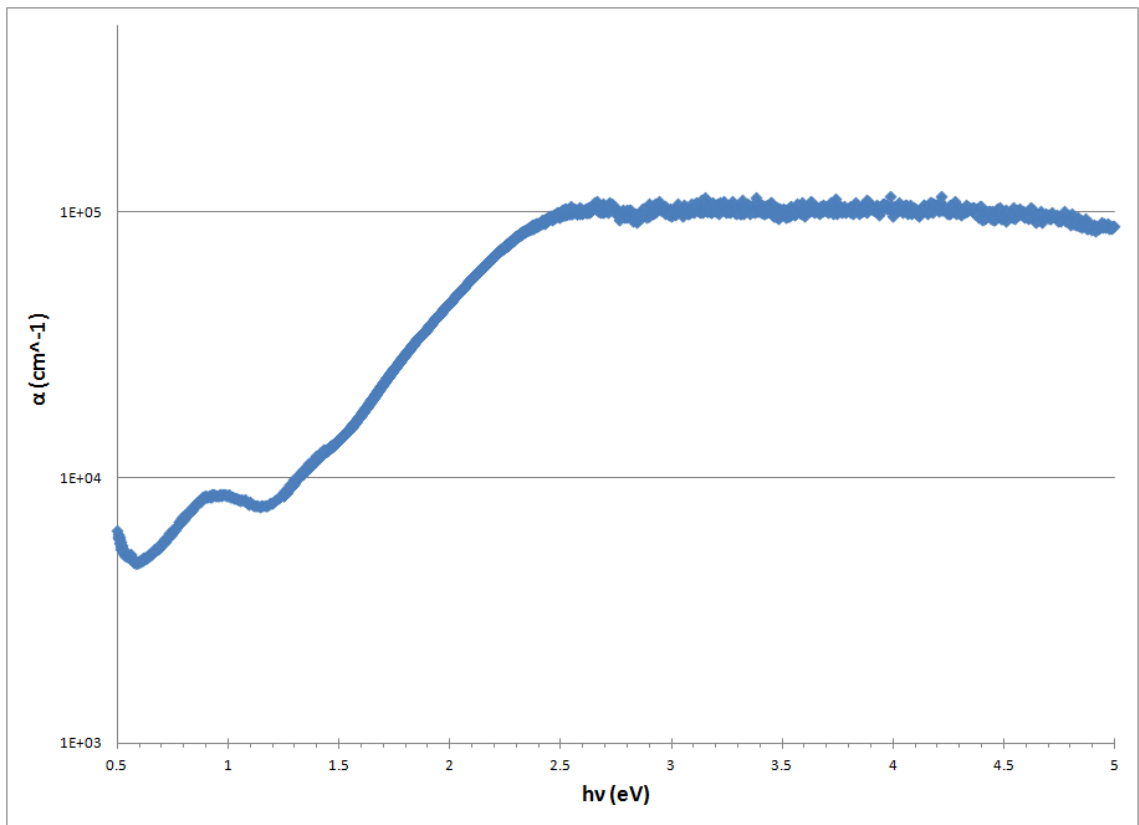


Figure 4.9: Measured absorption coefficient for a Cu_3PSe_4 thin-film sample.

were in the range of 19.8–30.3 cm²/V·s. Resistivities measured with the Hall effect measurement system (5.5–5.92 Ω·cm) are similar to those obtained by the four-point probe (5.0 Ω·cm).

4.4 Conclusion

This chapter describes the first thin-film research directed to the Cu₃PSe₄ material. The primary difficulty faced in this work was fabricating Cu₃PSe₄ thin films of sufficient quality for characterization. After a study of PLD process parameters failed to produce Cu₃PSe₄ thin-films as-deposited, post-deposition anneals were used to modify film stoichiometry. The best Cu₃PSe₄ thin-films were synthesized by annealing thin-film precursors containing Cu₇PSe₆ and Cu_{1.8}Se phases in the presence of P₄Se₃ powder at 200 °C for 1 hr.

Experimental results from Cu₃PSe₄ thin-film characterization support its use as a solar absorber material. Optical transmission and reflection measurements indicate absorption above the desired level of 10⁵ cm⁻¹, with an optical bandgap of ~1.2 eV. Electrical measurements indicate satisfactory mobility and carrier concentrations.

5. CuTaS₃ THIN FILMS

Although the crystal structure of copper tantalum trisulfide (CuTaS₃) was first determined in 1964, little work has been done on the material over its 58 year history. [67] No potential application existed until researchers at NREL identified CuTaS₃ as a potential solar absorber. Structural calculations indicating a bandgap of 1.37 eV and high optical absorption for CuTaS₃ formed the impetus for the thin-film synthesis and characterization presented in this chapter. The maximum efficiency of CuTaS₃ solar cells is projected to be greater than those currently achieved by leading thin-film solar cell technologies.

This chapter begins with an overview of previously known material properties of CuTaS₃. The crystal structure is presented, along with calculations supporting its suitability for solar absorption. A description of experiments performed in this thesis research follows. Lastly, experimental results are presented and analyzed.

5.1 Introduction

The crystal structure of CuTaS₃, as more accurately redetermined in 1987, is shown in Fig. 5.1. The structure is orthorhombic with lattice parameters $a = 9.488 \text{ \AA}$, $b = 3.486 \text{ \AA}$, and $c = 11.754 \text{ \AA}$. [12, 68] Chains of CuS₄ tetrahedra and TaS₆ octahedra link to form a honeycomb-like pattern with large channels in the [010] direction. [12, 69]

Figure 5.2 shows the calculated absorption coefficient (α) of CuTaS₃. A rapid turn-on in absorption is observed, with α exceeding 10^5 cm^{-1} within 0.5 eV of the bandgap. This further supports the material's promise as an effective solar absorber.

The spectroscopically limited maximum efficiency (SLME) of CuTaS₃ is shown as a function of absorber layer thickness in Fig. 5.3. For absorber layers over 500 nm in thickness the maximum efficiency exceeds 30% . Since this value is significantly higher than the currently achieved maximum efficiencies of the leading thin-film solar

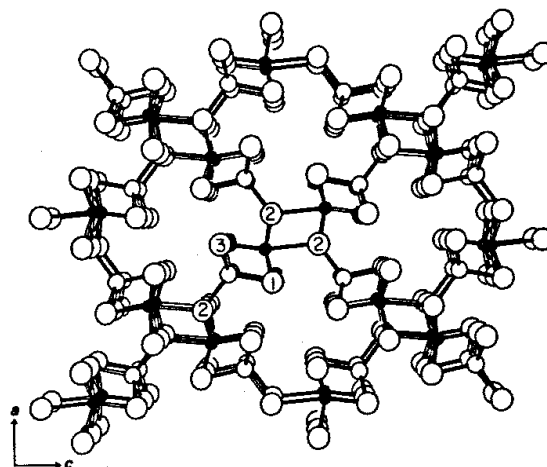


Figure 5.1: Crystal structure for CuTaS₃ showing Cu (small white circles), S (large white circles), and Ta (black dots). Large channels in the [010] direction are visible. [12]

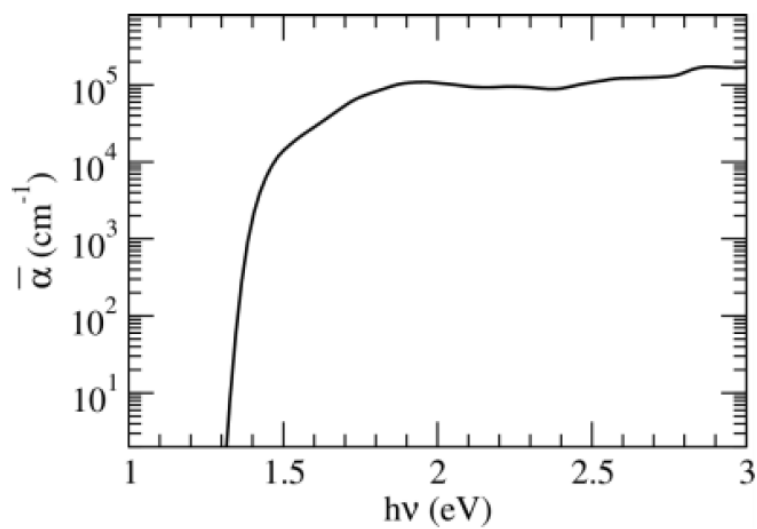
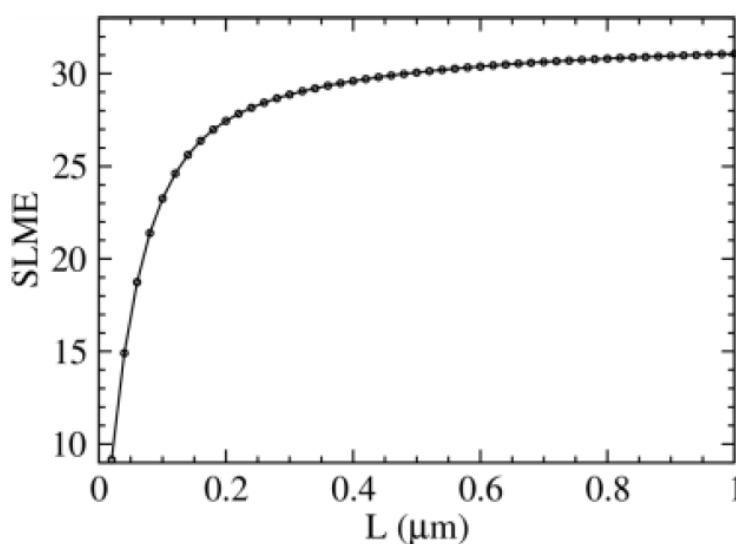


Figure 5.2: Calculated absorption coefficient for CuTaS₃. [11]

Table 5.1: Comparison of CuTaS₃ efficiency to leading thin-film solar cell technologies.

Absorber Material:	CdTe	CIGS	a-Si	CuTaS ₃
Efficiency:	16.5%	20%	15%	30% [†]
Absorber Thickness:	6 μm	2 μm	300 nm	500 nm [†]

[†] Potential maximum efficiency according to SLME calculations.

Figure 5.3: Calculated SLME for CuTaS₃. [11]

cell technologies, CuTaS₃ is a viable absorber material. Table 5.1 shows a comparison between the SLME for CuTaS₃ and reported maximum efficiencies achieved by CdTe, CIGS, and a-Si solar cells.

The above-mentioned background information provided the motivation for synthesis of CuTaS₃ thin-films. The remainder of this chapter illustrates the experimental procedures followed for successful thin-film fabrication, as well as the results of their electrical and optical characterization.

5.2 Experiment

Synthesis of CuTaS_3 thin-films was accomplished through modifying the procedures used previously to fabricate Cu_3TaS_4 at Oregon State University. [5] Three methods were attempted: sulfurization of Cu-Ta multilayer precursors, sulfurization of Cu-Ta quasi-alloy precursors, and electron-beam evaporation of CuTaS_3 pellets. All samples discussed in this chapter were deposited on fused silica substrates.

5.2.1 Sulfurization of Cu-Ta thin-film precursors

The process for sulfurizing Cu-Ta precursors is depicted in Fig. 5.4. Cu and Ta layers were deposited by either pulsed laser deposition (PLD) or electron-beam (e-beam) evaporation, with layer thicknesses chosen to provide an equal number of Cu and Ta atoms. This deposition was performed either (a) at room temperature to form multilayer structures, or (b) on substrates heated to 350°C to form uniformly mixed Cu-Ta *quasi-alloys* in which interdiffusion of Ta and Cu occurs and no layers are present. Sulfur was then introduced to the films (c) through post-deposition annealing with temperatures ranging from $400\text{--}800^\circ\text{C}$. Sealed tube anneals with excess S powder were primarily used, as well as tube furnace anneals under flowing H_2S gas with excess S powder.

PLD was used in initial experiments for deposition of Cu-Ta quasi-alloys. Laser fluence varied from $3.375\text{--}7.5\text{ J/cm}^2$, and laser repetition rate was 7 Hz. These large fluences are consistent with the high ablation threshold of metals. [34] Total film thicknesses were $\sim 133\text{ nm}$, deposited by alternating between pure Ta and Cu targets using a programmable looping routine editor built into the system. The most successful such experiment yielded films composed of 65% CuTaS_3 and 35% Cu_3TaS_4 , after a 6 hr sulfurizing anneal at 700°C .

E-beam evaporation was used as an alternative method for depositing Cu-Ta precursors over larger areas with improved control of film thickness, after precursors deposited

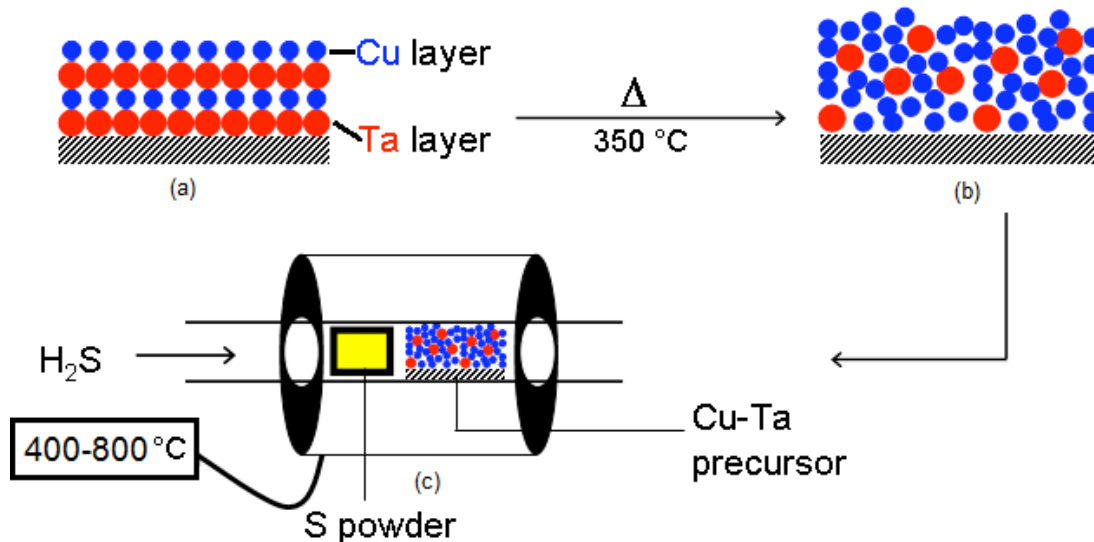


Figure 5.4: Process flow of sulfurization of CuTa precursors, showing (a) CuTa multilayers, (b) CuTa quasi-alloy, and (c) tube furnace sulfurization. Sealed tube anneals were also performed as an alternative to using the tube furnace.

by PLD demonstrated poor thickness uniformity over 1 cm^2 substrates. CuTaS_3 was successfully synthesized from post-deposition anneals of thin-film precursors deposited by e-beam evaporation, in which a 22 nm-thick layer of Cu was grown on a 40 nm-thick Ta layer at room temperature. The bilayer precursor was then sulfurized at 650 °C for 1 hr. Figure 5.5 shows the measured XRD spectrum. This experiment proved hard to reproduce as controlling the stoichiometry of the Cu-Ta precursors was difficult. In such multilayer precursors, Ta was deposited directly onto the substrate due to its use as a Cu diffusion barrier material. [70, 71]

5.2.2 Electron-beam evaporation of CuTaS_3 pellets

Previous work at Oregon State University demonstrated the best results in films made directly from phase-pure targets, rather than sulfurization of precursors. A pellet was fabricated which contained both CuTaS_3 and Cu_3TaS_4 phases. This pellet was used for electron beam evaporation to deposit thin-films at substrate temperatures varying from

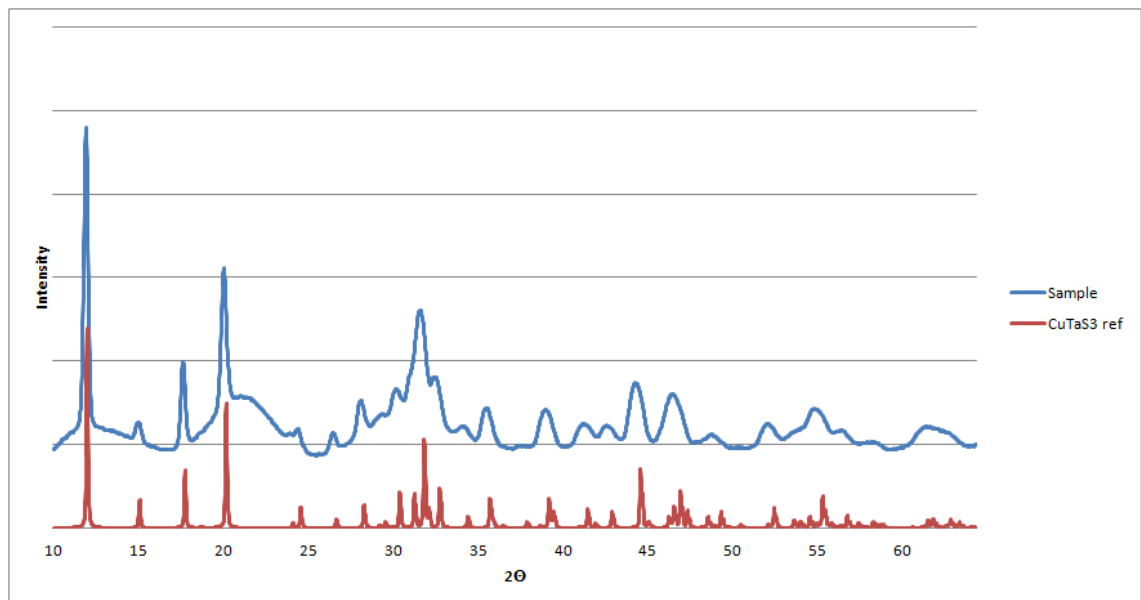


Figure 5.5: Measured XRD spectrum for CuTaS_3 sample (blue) with CuTaS_3 reference spectrum (red) shown for comparison. The sample was deposited by e-beam (40 nm Ta and 22 nm Cu) and then annealed in a S ambient.

room temperature (20 °C) to 300 °C. Depositions at room temperature yielded CuS and those performed at 300 °C produced $\text{Cu}_{1.8}\text{S}$. In both cases, the refractory metal Ta was not successfully evaporated from the pellet.

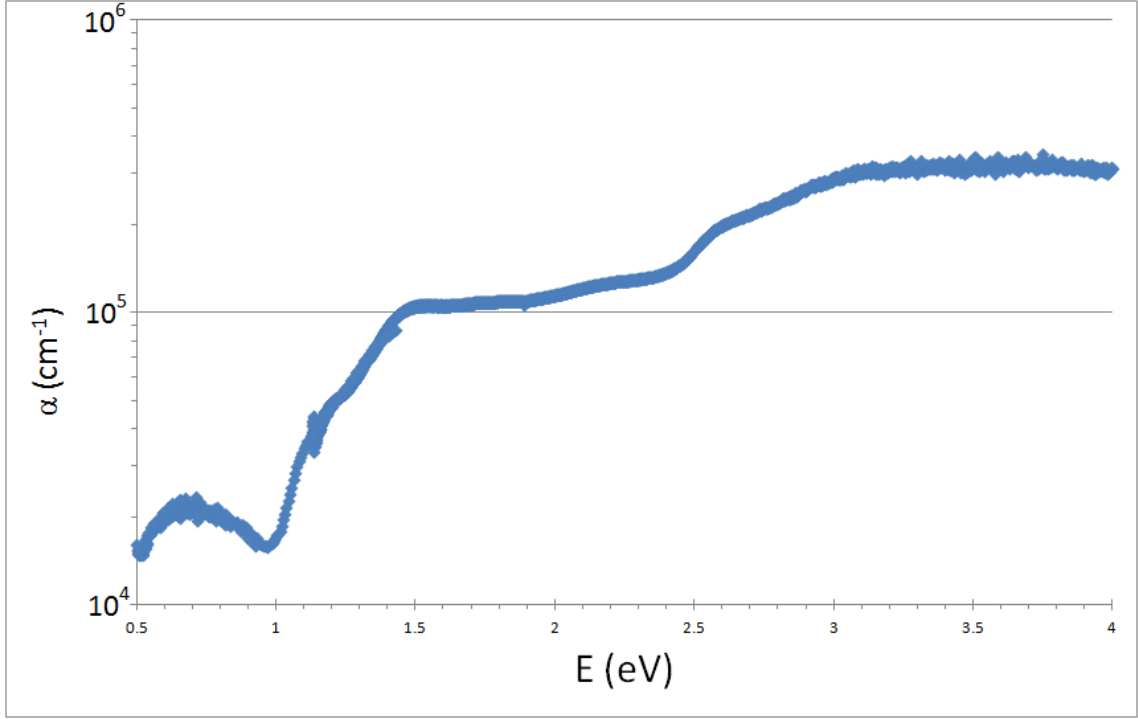


Figure 5.6: Measured absorption coefficient (α) for a CuTaS_3 thin-film sample prepared by sulfurization of a Cu-Ta multilayer precursor.

5.3 Results

Figure 5.6 shows the absorption coefficient for a CuTaS_3 thin-film, determined by optical transmission and reflection measurements. The optical bandgap, indicated by the onset of absorption, occurs at approximately 1 eV. This value is lower than the calculated bandgap for CuTaS_3 (1.32 eV), and is barely within the range of acceptable bandgaps for solar absorbers ($\sim 1\text{--}1.6$ eV). [26, 27, 28, 30] The turn-on of absorption is sufficiently rapid, with α reaching 10^5 cm^{-1} within 0.5 eV of the bandgap. A simple two probe conductivity test of the film demonstrated insulating behavior, so Hall effect measurements were not performed.

5.4 Conclusion

The research presented in this chapter constitutes the entirety of all work performed on CuTaS₃ thin-films to date. Successful fabrication of CuTaS₃ thin-films was demonstrated, although they proved excessively difficult to reproduce. It is speculated that this difficulty results from the variability of the Cu-Ta precursor stoichiometry. Growth rates for Cu and Ta thin-films deposited by e-beam evaporation were frequently recalibrated, but with limited success.

Optical characterization of CuTaS₃ samples showed strong absorption ($\alpha > 10^5 \text{ cm}^{-1}$). The observed optical bandgap was less than ideal ($\sim 1 \text{ eV}$), but may still be acceptable for a solar absorber. The insulating behavior of thin films is suspected to be due to the poor quality of the films produced to date. This may possibly be improved by varying precursor layering schemes or anneal process parameters. The predicted suitability of CuTaS₃ for solar absorber applications cannot be fully confirmed without validating electrical characterization results.

6. CONCLUSIONS AND RECOMMENDATIONS FOR FUTURE WORK

6.1 Conclusions

The aim of this research work was to fabricate and characterize thin-films of potential solar absorber materials. Two ternary chalcogenides, Cu_3PSe_4 and CuTaS_3 , were selected for their calculated absorption properties, elemental abundance, and non-toxicity. Both materials were successfully fabricated by post-deposition anneals performed on thin-film precursors deposited by PVD techniques. Characterization of the synthesized thin-films demonstrated high optical absorption as predicted by structural calculations.

6.1.1 Cu_3PSe_4

Cu_3PSe_4 thin-films were synthesized by post-deposition anneals of films deposited by PLD. The best results were achieved by annealing films containing both Cu_7PSe_6 and $\text{Cu}_{1.8}\text{Se}$ phases, after PLD failed to produce Cu_3PSe_4 directly. Initial successes resulted from annealing in the presence of P and Se powders at 450 °C, but film quality was improved by annealing with P_4Se_3 powder at a lower temperature (200 °C).

Characterization of Cu_3PSe_4 thin-films supports the material's use as a solar absorber. Optical transmission and reflection measurements show absorption above the desired level of 10^5 cm^{-1} , with an optical bandgap of $\sim 1.2 \text{ eV}$. Hall effect measurements indicate appropriate Hall mobility and carrier concentrations of 19.8–30.3 $\text{cm}^2/\text{V}\cdot\text{s}$ and $3.3\text{--}4.9 \times 10^{16} \text{ cm}^{-3}$, respectively.

6.1.2 CuTaS₃

The research presented in this thesis is the first study of CuTaS₃ thin films, and appears to constitute the majority of all research ever performed on the material itself. Phase-pure thin-films proved exceedingly difficult to reproduce. This is consistent with previous work at OSU using similar techniques on related materials. [5] Even with frequent calibration of Cu and Ta growth rates for films deposited by e-beam evaporation, thin-film precursors are suspected to have variable uncontrolled Cu-Ta ratios. Success was achieved by annealing Cu-Ta bilayer precursors consisting of 22 nm Cu on 40 nm Ta in the presence of S powder at 650 °C for 1 hr. E-beam evaporation of a polycrystalline pellet containing CuTaS₃ and Cu₃TaS₄ was also attempted, although films produced in this manner were extremely Ta-deficient.

CuTaS₃ thin-films were too insulating for electrical characterization to be performed. However, optical transmission and reflection measurements indicated promising absorbing behavior, with the absorption coefficient (α) exceeding 10^5 cm^{-1} within 0.5 eV of the bandgap. The measured optical bandgap was less than desired, at $\sim 1 \text{ eV}$.

6.2 Recommendations for future work

The research presented here forms the background for future work using Cu₃PSe₄ and CuTaS₃ as solar absorbers. This section summarizes the next steps along the path towards utilizing these materials for working PV devices.

6.2.1 Cu₃PSe₄

Further electrical characterization should be performed on Cu₃PSe₄ thin-films, including PEC cell measurements. This would provide values for short-circuit current, open-circuit voltage, fill factor, and cell conversion efficiency. Comparison to the calculated SLME would then be possible.

Future use of Cu_3PSe_4 as an absorber layer in thin-film solar cells will benefit from larger-area coverage than is presently achieved with PLD. In some cases, Cu_3PSe_4 thin-films were achieved by annealing phase-pure $\text{Cu}_{1.8}\text{Se}$ precursors. This suggests the possibility of depositing Cu-Se multilayer or alloy precursors by sputtering or e-beam evaporation. Cu-Se sputter targets are presently commercially available. It should be determined whether annealing sputtered Cu-Se precursors can successfully produce Cu_3PSe_4 thin-films.

6.2.2 CuTaS_3

Future work on CuTaS_3 thin films will require a modification of the fabrication process to improve the yield of sulphurization attempts. Since past work at Oregon State University employed several different methods for synthesizing Cu_3TaS_4 thin-films, attention should be given to exploring such alternatives. [5] These methods include the sulphurization of both Cu-Ta quasi-alloys and Cu-Ta multilayers consisting of more than two layers. If an e-beam target with density $>90\%$ can be acquired, then depositing CuTaS_3 directly by that method would be attractive alternative to the sulphurization anneal.

Electrical characterization is critical to further support the use of CuTaS_3 as a solar absorber. Higher quality thin-films with low resistivity are necessary, and will likely result from an improved recipe for synthesis. Hall effect measurements should be performed to determine carrier mobility and concentration. Efforts should be made to increase the bandgap of CuTaS_3 by substituting V on a Ta site, or Ag on a Cu site.

BIBLIOGRAPHY

1. S. J. Fonash, *Solar cell device physics*. Oxford: Elsevier Inc., 2010.
2. T. Markvart and L. Castaner, *Practical handbook of photovoltaics: fundamentals and applications*. New York: Elsevier Ltd., 2003.
3. P. A. Hersh, *Wide band gap semiconductors and insulators: synthesis, processing and characterization*. PhD thesis, Oregon State University, October 2007.
4. J. Nelson, *The physics of solar cells*. London: Imperial College Press, 2003.
5. P. F. Newhouse, *Growth and characterization of widegap semiconducting oxide and chalcogenide thin films by pulsed laser deposition*. PhD thesis, Oregon State University, September 2008.
6. D. L. Smith, *Thin-film deposition: principles and practice*. New York: McGraw Hill, 1995.
7. B. B. He, *Two-dimensional x-ray diffraction*. New Jersey: John Wiley & Sons, Inc., 2009.
8. M. S. Tyagi, *Introduction to semiconductor materials and devices*. New York: John Wiley & Sons, Inc., 1991.
9. E. Bontempi, "X-ray reflectivity for the characterization of thin films," *Recent Research Developments in Chemical Physics*, vol. 5, pp. 461–488, 2004.
10. D. H. Foster, V. Jieratum, R. Kykyneshi, D. A. Keszler, and G. Schneider, "Electronis and optical properties of potential solar absorber Cu_3PSe_4 ," *Applied Physics Letters*, vol. 99, 2011.
11. L. Yu, "Material calculations." Unpublished results, January 2012.
12. S. A. Sunshine and J. A. Ibers, "Redetermination of the structures of CuTaS_3 and Nb_2Se_9 ," *Acta Crystallographica*, vol. C43, pp. 1019–1022, 1987.
13. P. Bhattacharya, *Semiconductor optoelectronic devices*. Englewood Cliffs, New Jersey: Prentice-Hall, Inc., 1994.
14. R. F. Pierret, *Semiconductor device fundamentals*. Massachusetts: Addison-Wesley Publishing Company, Inc., 1996.
15. D. Abou-Ras, T. Kirchartz, and U. Rau, *Advanced characterization techniques for thin film solar cells*. Germany: Wiley-VCH, 2011.

16. A. Facchetti and T. J. Marks, *Transparent electronics: from synthesis to applications*. United Kingdom: John Wiley & Sons Ltd, 2010.
17. A. Nussbaum and R. A. Phillips, *Contemporary optics for scientists and engineers*. New Jersey: Prentice-Hall, Inc., 1976.
18. S. Sze and K. K. Ng, *Physics of semiconductor devices, third edition*. New Jersey: John Wiley & Sons, Inc., 2007.
19. C. M. Wolfe, J. Nick Holonyak, and G. E. Stillman, *Physical properties of semiconductors*. New Jersey: Prentice Hall, 1989.
20. J. S. Blakemore, *Semiconductor statistics*. Toronto: General Publishing Company, 1987.
21. W. Shockley and H. J. Queisser, "Detailed balance limit of efficiency of p-n junction solar cells," *Journal of Applied Physics*, vol. 32, pp. 510–519, 1961.
22. A. Luque and S. Hegedus, *Handbook of photovoltaic science and engineering*. England: John Wiley & Sons Ltd, 2003.
23. D. K. Schroder, *Semiconductor material and device characterization*. New Jersey: John Wiley & Sons, Inc., 2006.
24. R. E. Hummel, *Electronic properties of materials*. New York: Springer-Verlag, 1985.
25. S. Demtsu and J. Sites, "Effect of back-contact barrier on thin-film CdTe solar cells," *Thin Solid Films*, vol. 510, pp. 320–324, 2006.
26. J. Poortmans and V. Arkhipov, *Thin film solar cells fabrication, characterization and applications*. England: John Wiley & Sons Ltd., 2006.
27. D. B. Mitzi, O. Gunawan, T. K. Todorov, K. Wang, and S. Guha, "The path towards a high-performance solution-processed kesterite solar cell," *Solar Energy Materials & Solar Cells*, vol. 95, pp. 1421–1436, 2011.
28. L. Yu and A. Zunger, "Identification of potential photovoltaic absorbers based on first-principles spectroscopic screening of materials," *Physical Review Letters*, vol. 108, pp. 068701–1–068701–5, 2012.
29. X. Wu, "High-efficiency CTO/ZTO/CdS/CdTe polycrystalline thin-film solar cells," *NREL*, 2001.
30. M. C. Lux-Steiner, "Non-conventional semiconductor materials for solar cells," *Springer Proceedings in Physics*, vol. 54, pp. 420–431, 1991.

31. I. Kaiser, K. Ernst, C. Fischer, R. Konenkamp, C. Rost, I. Sieber, and M. Lux-Steiner, "The eta-solar cell with CuInS_2 : a photovoltaic cell concept using an extremely thin absorber (eta)," *Solar Energy Materials & Solar Cells*, vol. 67, pp. 89–96, 2001.
32. D. A. Barkhouse, O. Gunawan, T. Gokmen, T. K. Todorov, and D. B. Mitzi, "Device characteristics of a 10.1% hydrazine-processed $\text{Cu}_2\text{ZnSn}(\text{Se,S})_4$ solar cell," *Progress in Photovoltaics: Research & Applications*, vol. 20, pp. 6–11, 2012.
33. O. Gunawan, T. K. Todorov, and D. B. Mitzi, "Loss mechanisms in hydrazine-processed $\text{Cu}_2\text{ZnSn}(\text{Se,S})_4$ solar cells," *Applied Physics Letters*, vol. 97, pp. 233506–233506–3, 2010.
34. D. B. Chrisey and G. K. Hubler, *Pulsed laser deposition of thin films*. New York: John Wiley & Sons, 1994.
35. P. Atkins, *Shriver and Atkins' inorganic chemistry, fifth edition*. Great Britain: Oxford University Press, 2010.
36. R. Kykyneshi, *Pulsed laser deposition and thin film properties of p-type BaCuSF, BaCuSeF, BaCuTeF and n-type $\text{Zn}_2\text{In}_2\text{O}_5$ wide band-gap semiconductors*. PhD thesis, Oregon State University, 2007.
37. J. T. Cheung and H. Sankur, "Growth of thin films by laser-induced evaporation," vol. 15, no. 1, 1988.
38. A. Elshabini-Riad and F. D. B. III, *Thin film technology handbook*. New York: McGraw Hill, 1997.
39. K. J. Kuhn, *Laser engineering*. New Jersey: Prentice-Hall, 1998.
40. A. Zakutayev, *BaCuChF (Ch = S, Se, Te) p-type transparent conductors*. PhD thesis, Oregon State University, 2010.
41. S. Wolf and R. N. Tauber, *Silicon processing for the VLSI era, volume 1: process technology*. California: Lattice Press, 2000.
42. J. A. Spies, "Inorganic thin-film solar cells," Master's thesis, Oregon State University, 2007.
43. D. M. Mattox and G. J. Kominiak, "Structure modification by ion bombardment during deposition," *The Journal of Vacuum Science and Technology*, vol. 9, pp. 528–532, 1971.
44. J. P. Bender, *Manufacture and characterization of novel actfel materials and devices*. PhD thesis, Oregon State University, 2003.

45. R. L. Hoffman, "Development, fabrication, and characterization of transparent electronic devices," Master's thesis, Oregon State University, June 2002.
46. A. P. Sutton, *Electronic structure of materials*. New York: Oxford University Press, 1993.
47. R. H. Bube, *Electronic properties of crystalline solids*. New York: Academic Press, Inc., 1974.
48. E. Altschul, *Ocean Optics System User Guide to measuring absorbance of a thin film sample*. 2011.
49. I. Kojima and B. Li, "Structural characterization of thin films by x-ray reflectivity," *The Rigaku Journal*, vol. 16, pp. 31–42, 1999.
50. M. Cladek, V. Valvoda, C. Dorner, C. Holy, and J. Grim, "Quantitative study of interface roughness replication in multilayers using x-ray reflectivity and transmission electron microscopy," *Applied Physics Letter*, vol. 69, pp. 1318–1320, 1996.
51. L. G. Parratt, "Surface studies of solids by total reflection of x-rays," *Physical Review*, vol. 95, pp. 359–369, 1954.
52. H. Fujiwara, *Spectroscopic ellipsometry: principles and applications*. New Jersey: John Wiley & Sons, Inc., 2007.
53. J. N. Hilfiker, C. L. Bungay, R. A. Synowicki, T. E. Tiwald, C. M. Herzinger, B. Johs, G. K. Pribil, and J. A. Woollam, "Progress in spectroscopic ellipsometry: Applications from vacuum ultraviolet to infrared," *Journal of Vacuum Science and Technology*, vol. 21, pp. 1103–1108, 2003.
54. C. R. Brundle, J. Charles A Evans, and S. Wilson, *Encyclopedia of materials characterization*. Massachusetts: Butterworth-Heinemann, 1992.
55. H. G. Tompkins and E. A. Irene, *Handbook of ellipsometry*. New York: William Andrew, Inc., 2005.
56. M. Gratzel, "Photoelectrochemical cells," *Nature*, vol. 414, pp. 338–344, 2001.
57. S. M. Boudreau, R. D. Rauh, and R. A. Boudreau, "A photoelectrochemical solar cell," *Journal of Chemical Education*, vol. 60, pp. 498–499, 1983.
58. J. Garin and E. Parthe, "The crystal structure of Cu_3PSe_4 and other ternary normal tetrahedral structure compounds with composition I_3Se_4 ," *Acta Crystallographica*, vol. 28, pp. 3672–3674, 1972.
59. V. Jieratum, R. S. Kokenyesi, A. J. Ritenour, L. N. Zakharov, S. W. Boettcher, J. F. Wager, and D. A. Keszler, "Earth abundant Cu-based chalcogenides for photovoltaic cells." unpublished results, 2012.

60. J. V. Marzik, A. K. Hsieh, K. Dwight, and A. Wold, "Photoelectronic properties of Cu_3PS_4 and $\text{Cu}_3\text{PS}_3\text{Se}$ single crystals," *Journal of Solid State Chemistry*, vol. 49, pp. 43–50, 1983.
61. S. Russell, S. Rafalski, R. Spreitzer, J. Li, M. Moinpour, F. Moghadam, and T. Alford, "Enhanced adhesion of copper to dielectrics via titanium and chromium additions and sacrificial reactions," *Thin Solid Films*, vol. 262, pp. 154–167, 1995.
62. H. B. Michaelson, "The work function of the elements and its periodicity," *Journal of Applied Physics*, vol. 48, pp. 4729–4733, 1977.
63. W.-Q. Wang, I. Raaijmakers, B. J. Burrow, S. Suthar, and S. Redkar, "Reactively sputtered TiN as a diffusion barrier between Cu and Si," *Journal of Applied Physics*, vol. 68, pp. 5176–5187, 1990.
64. J. Uhm and H. Jeon, "TiN diffusion barrier grown by atomic layer deposition method for Cu metallization," *Japanese Journal of Applied Physics*, vol. 40, pp. 4657–4660, 2001.
65. S.-K. Rha, W.-J. Lee, S.-Y. Lee, Y.-S. Hwang, Y.-J. Lee, D.-I. Kim, D.-W. Kim, S.-S. Chun, and C.-O. Park, "Improves TiN film as a diffusion barrier between copper and silicon," *Thin Solid Films*, vol. 320.
66. R. Maxwell and H. Echert, "Chemical equilibria in glass-forming melts: high temperature ^{31}P and ^{77}Se NMR of the phosphorus-selenium system," *Journal of the American Chemical Society*, vol. 116, pp. 682–689, 1994.
67. C. Crevecoeur and C. Romers, "The crystal structure of CuTaS_3 ," *Proceedings of the Koninklijke Nederlandse Akademie van Wetenschappen, Series B: Physical Sciences*, vol. 67, pp. 289–291, 1964.
68. S. A. Sunshine, *Synthesis and characterization of new low dimensional transition metal chalcogenides*. PhD thesis, Northwestern University, 1987.
69. P. J. Squattrito, P. N. Swepston, and J. A. Ibers, "Crystal structure of the new ternary chalcogenide $\text{Ta}_2\text{Cu}_{0.80}\text{S}_6$. relationship to known copper and tantalum chalcogenides," *Inorganic Chemistry*, vol. 26, pp. 1187–1188, 1987.
70. T. Laurila, K. Zeng, J. Kivilahti, J. Molarius, and I. Suni, "Chemical stability of Ta diffusion barrier between Cu and Si," *Thin Solid Films*, vol. 373, pp. 64–67, 2000.
71. K. Holloway, P. M. Fryer, J. Cyril Cabral, J. M. E. Harper, P. J. Bailey, and K. H. Kelleher, "Tantalum as a diffusion barrier between copper and silicon: failure mechanism and effect of nitrogen additions," *Journal of Applied Physics*, vol. 71, pp. 5433–5444, 1992.